

Chapter 12

Surface plasmons

12.1 Introduction

The interaction of metals with electromagnetic radiation is largely dictated by the free conduction electrons in the metal. According to the simple Drude model, the free electrons oscillate 180° out of phase relative to the driving electric field. As a consequence, most metals possess a negative dielectric constant at optical frequencies which causes e.g. a very high reflectivity. Furthermore, at optical frequencies the metal's free electron gas can sustain surface and volume charge density oscillations, called plasmon polaritons or plasmons with distinct resonance frequencies. The existence of plasmons is characteristic for the interaction of metal nanostructures with light. Similar behavior cannot be simply reproduced in other spectral ranges using the scale invariance of Maxwell's equations since the material parameters change considerably with frequency. Specifically, this means that model experiments with e.g. microwaves and correspondingly larger metal structures cannot replace experiments with metal nanostructures at optical frequencies. The surface charge density oscillations associated with surface plasmons at the interface between a metal and a dielectric can give rise to strongly enhanced optical near-fields which are spatially confined to the interface. Similarly, if the electron gas is confined in three dimensions, as in the case of a small subwavelength particle, the overall displacement of the electrons with respect to the positively charged lattice leads to a restoring force which in turn gives rise to specific particle plasmon resonances depending on the geometry of the particle. In particles of suitable (usually pointed) shape, extreme local charge accumulations can occur that are accompanied by strongly enhanced optical fields.

The study of optical phenomena related to the electromagnetic response of metals has been recently termed as *plasmonics* or *nanoplasmonics*. This rapidly growing field of nanoscience is mostly concerned with the control of optical radiation on the subwavelength scale. Many innovative concepts and applications of metal optics have

been developed over the past few years and in this chapter we will discuss a few examples. We will first review the optical properties of noble metal structures of various shapes, ranging from two-dimensional thin films to one and zero dimensional wires and dots, respectively. The analysis will be based on Maxwell's equations using the metal's frequency dependent complex dielectric function. Since most of the physics of the interaction of light with metal structures is hidden in the frequency dependence of the metal's complex dielectric function, we will begin with a discussion of the fundamental optical properties of metals. We will then turn to important solutions of Maxwell's equations for noble metal structures, i.e. the plane metal-dielectric interface and subwavelength metallic wires and particles that show a resonant behavior. Finally, and where appropriate during the discussion, applications of surface plasmons in nano-optics will be discussed. As *nanoplasmonics* is a very active field of study we can expect that many new applications will be developed in the years to come and that dedicated texts will be published. Finally, it should be noted that optical interactions similar to those discussed here are, also encountered for infrared radiation interacting with polar materials. The corresponding excitations are called surface phonon polaritons.

12.2 Optical properties of noble metals

The optical properties of metals and noble metals in particular have been discussed by numerous authors [1-3]. We give here a short account with emphasis on the classical pictures of the physical processes involved. The optical properties of metals can be described by a complex dielectric constant that depends on the frequency of the light (see chapter 2). The optical properties of metals are determined mainly (i) by the fact that the conduction electrons can move freely within the bulk of material and (ii) that interband excitations can take place if the energy of the photons exceeds the band gap energy of the respective metal. In the picture we adopt here, the presence of an electric field leads to a displacement \mathbf{r} of an electron which is associated with a dipole moment $\boldsymbol{\mu}$ according to $\boldsymbol{\mu} = e\mathbf{r}$. The cumulative effect of all individual dipole moments of all free electrons results in a macroscopic polarization per unit volume $\mathbf{P} = n\boldsymbol{\mu}$, where n is the number of electrons per unit volume. As discussed in chapter 2, the electric displacement \mathbf{D} is related to this macroscopic polarization by

$$\mathbf{D}(\mathbf{r}, t) = \varepsilon_0 \mathbf{E}(\mathbf{r}, t) + \mathbf{P}(\mathbf{r}, t) . \quad (12.1)$$

Furthermore, also the constitutive relation

$$\mathbf{D} = \varepsilon_0 \varepsilon \mathbf{E} \quad (12.2)$$

was introduced. Using (12.1) and (12.2), assuming an isotropic medium, the dielectric constant can be expressed as [2, 4]

$$\varepsilon = 1 + \frac{|\mathbf{P}|}{\varepsilon_0 |\mathbf{E}|} \quad (12.3)$$

The displacement \mathbf{r} and therefore the macroscopic polarization \mathbf{P} can be obtained by solving the equation of motion of the electrons under the influence of an external field.

12.2.1 Drude-Sommerfeld theory

As a starting point, we consider only the effects of the free electrons and apply the Drude-Sommerfeld model for the free-electron gas (see e.g. [5]).

$$m_e \frac{\partial^2 \mathbf{r}}{\partial t^2} + m_e \Gamma \frac{\partial \mathbf{r}}{\partial t} = e \mathbf{E}_0 e^{-i\omega t} \quad (12.4)$$

where e and m_e are the charge and the effective mass of the free electrons, and \mathbf{E}_0 and ω are the amplitude and the frequency of the applied electric field. Note that the equation of motion contains no restoring force since free electrons are considered. The damping term is proportional to $\Gamma = v_F/l$ where v_F is the Fermi velocity and l is the electrons mean free path between scattering events. Solving (12.4) using the

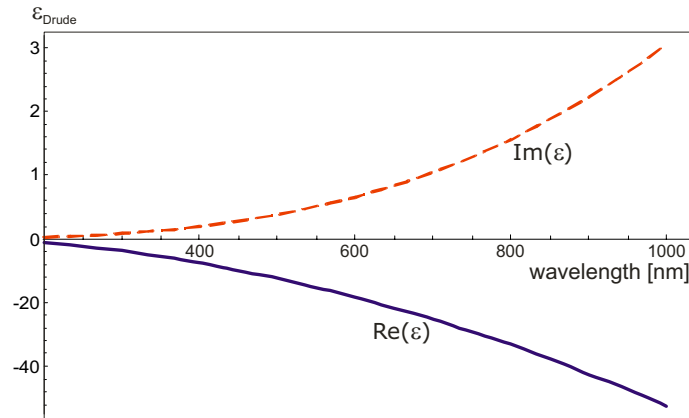


Figure 12.1: Real and imaginary part of the dielectric constant for gold according to the Drude-Sommerfeld free electron model ($\omega_p = 13.8 \cdot 10^{15} \text{ s}^{-1}$, $\Gamma = 1.075 \cdot 10^{14} \text{ s}^{-1}$). The blue solid line is the real part, the red, dashed line is the imaginary part. Note the different scales for real and imaginary part.

Ansatz $\mathbf{r}(t) = \mathbf{r}_0 e^{-i\omega t}$ and using the result in (12.3) yields

$$\varepsilon_{\text{Drude}}(\omega) = 1 - \frac{\omega_p^2}{\omega^2 + i\Gamma\omega} . \quad (12.5)$$

Here $\omega_p = \sqrt{ne^2/(m_e\varepsilon_0)}$ is the volume plasma frequency. Expression (12.5) can be divided into real and imaginary parts as follows

$$\varepsilon_{\text{Drude}}(\omega) = 1 - \frac{\omega_p^2}{\omega^2 + \Gamma^2} + i \frac{\Gamma\omega_p^2}{\omega(\omega^2 + \Gamma^2)} \quad (12.6)$$

Using $\omega_p = 13.8 \cdot 10^{15} \text{ s}^{-1}$ and $\Gamma = 1.075 \cdot 10^{14} \text{ s}^{-1}$ which are the values for gold [4] the real and the imaginary parts of the dielectric function (12.6) are plotted in Fig. 12.1 as a function of the wavelength over the extended visible range. We note that the real part of the dielectric constant is negative over the extended visible range. One obvious consequence of this behavior is the fact that light can penetrate a metal only to a very small extent since the negative dielectric constant leads to a strong imaginary part of the refractive index $n = \sqrt{\varepsilon}$. Other consequences will be discussed later. The imaginary part of ε describes the dissipation of energy associated with the motion of electrons in the metal (see problem 12.1).

12.2.2 Interband transitions

Although the Drude-Sommerfeld model gives quite accurate results for the optical properties of metals in the infrared regime, it needs to be supplemented in the visible

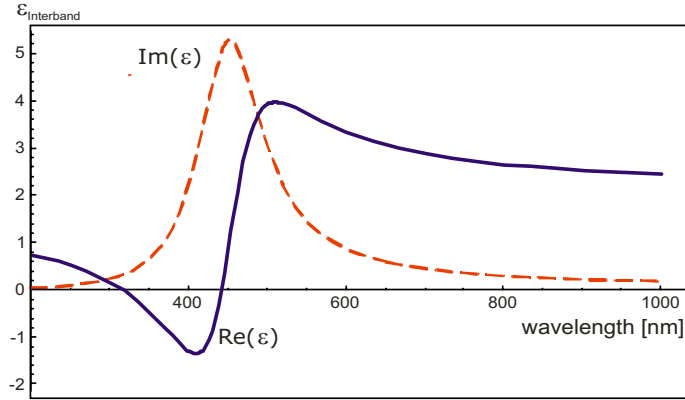


Figure 12.2: Contribution of bound electrons to the dielectric function of gold. The parameters used are $\tilde{\omega}_p = 45 \cdot 10^{14} \text{ s}^{-1}$, $\gamma = 8.35 \cdot 10^{-16} \text{ s}^{-1}$, and $\omega_0 = 2\pi c/\lambda$, with $\lambda = 450 \text{ nm}$. The solid blue line is the real part, the dashed red curve is the imaginary part of the dielectric function due to bound electrons.

range by the response of bound electrons. For example for gold, at a wavelength shorter than ~ 550 nm the measured imaginary part of the dielectric function increases much more strongly as predicted by the Drude-Sommerfeld theory. This is because higher energy photons can promote electrons of lower-lying bands into the conduction band. In a classical picture such transitions may be described by exciting the oscillation of bound electrons. Bound electrons in metals exist e.g. in lower-lying shells of the metal atoms. We apply the same method that was used above for the free electrons to describe the response of the bound electrons. The equation of motion for a bound electron reads as

$$m \frac{\partial^2 \mathbf{r}}{\partial t^2} + m\gamma \frac{\partial \mathbf{r}}{\partial t} + \alpha \mathbf{r} = e \mathbf{E}_0 e^{-i\omega t} . \quad (12.7)$$

Here, m is the *effective* mass of the bound electrons, which is in general different from the effective mass of a free electron in a periodic potential, γ is the damping constant describing mainly radiative damping in the case of bound electrons, and α is the spring constant of the potential that keeps the electron in place. Using the same Ansatz as before we find the contribution of bound electrons to the dielectric function

$$\varepsilon_{\text{Interband}}(\omega) = 1 + \frac{\tilde{\omega}_p^2}{(\omega_0^2 - \omega^2) - i\gamma\omega} . \quad (12.8)$$

Here $\tilde{\omega}_p = \sqrt{\tilde{n}e^2/m\varepsilon_0}$ with \tilde{n} being the density of the bound electrons. $\tilde{\omega}_p$ is introduced in analogy to the plasma frequency in the Drude-Sommerfeld model, however, obviously here with a different physical meaning and $\omega_0 = \sqrt{\alpha/m}$. Again we can rewrite (12.8) to separate the real and imaginary parts

$$\varepsilon_{\text{Interband}}(\omega) = 1 + \frac{\tilde{\omega}_p^2(\omega_0^2 - \omega^2)}{(\omega_0^2 - \omega^2)^2 + \gamma^2\omega^2} + i \frac{\gamma\tilde{\omega}_p^2\omega}{(\omega_0^2 - \omega^2)^2 + \gamma^2\omega^2} . \quad (12.9)$$

Fig. 12.2 shows the contribution to the dielectric constant of a metal* that derives from bound electrons. A clear resonant behavior is observed for the imaginary part and a dispersion-like behavior is observed for the real part. Fig. 12.3 is a plot of the dielectric constant (real and imaginary part) taken from the paper of Johnson & Christy [6] for gold (open circles). For wavelengths above 650 nm the behavior clearly follows the Drude-Sommerfeld theory. For wavelength below 650 nm obviously interband transitions become significant. One can try to model the shape of the curves by adding up the free-electron [Eq. (12.6)] and the interband absorption contributions [Eq. (12.9)] to the complex dielectric function (squares). Indeed, this much better reproduces the experimental data apart from the fact that one has to introduce a constant offset ε_∞ to (12.6) which accounts for the integrated effect of all higher-energy interband transition not considered in the present model (see e.g. [7]). Also,

*This theory naturally also applies for the behavior of dielectrics and the dielectric response of over a broad frequency range consists of several absorption bands related to different electromagnetically excited resonances [2].

since only one interband transition is taken into account, the model curves still fail to reproduce the data below ~ 500 nm.

12.3 Surface plasmon polaritons at plane interfaces

By definition surface plasmons are the quanta of surface-charge-density oscillations, but the same terminology is commonly used for collective oscillations in the electron density at the surface of a metal. The surface charge oscillations are naturally cou-

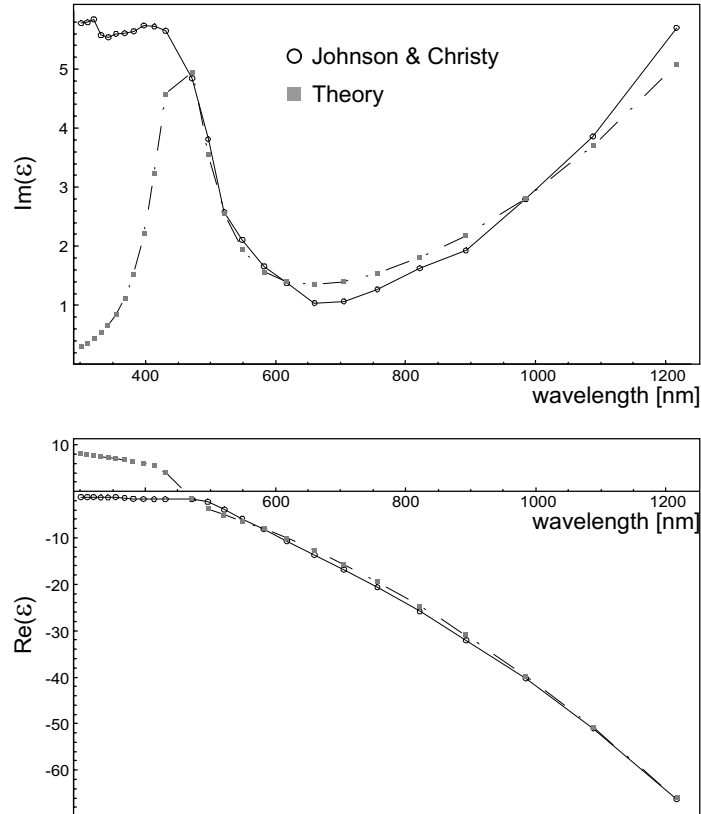


Figure 12.3: Dielectric function of gold: Experimental values and model. Upper panel: Imaginary part. Lower panel: Real part. Open circles: experimental values taken from [6]. Squares: Model of the dielectric function taking into account the free electron contribution and the contribution of a single interband transition. Note the different scales for the abscissae.

pled to electromagnetic waves which explains their designation as polaritons. In this section, we consider a plane interface between two media. One medium is characterized by a general, complex frequency-dependent dielectric function $\varepsilon_1(\omega)$ whereas the dielectric function of the other medium $\varepsilon_2(\omega)$ is assumed to be real. We choose the interface to coincide with the plane $z = 0$ of a Cartesian coordinate system (see Fig. 12.4). We are looking for *homogeneous* solutions of Maxwell's equations that are localized at the interface. A homogeneous solution is an eigenmode of the system, i.e. a solution that exists without external excitation. Mathematically, it is the solution of the wave equation

$$\nabla \times \nabla \times \mathbf{E}(\mathbf{r}, \omega) - \frac{\omega^2}{c^2} \varepsilon(\mathbf{r}, \omega) \mathbf{E}(\mathbf{r}, \omega) = 0, \quad (12.10)$$

with $\varepsilon(\mathbf{r}, \omega) = \varepsilon_1(\omega)$ if $z < 0$ and $\varepsilon(\mathbf{r}, \omega) = \varepsilon_2(\omega)$ if $z > 0$. The localization at the interface is characterized by electromagnetic fields that exponentially decay with increasing distance to the interface into both half spaces. It is sufficient to consider only p-polarized waves in both halfspaces because no solutions exist for the case of s-polarization (see problem 12.2).

P-polarized plane waves in halfspace $j = 1$ and $j = 2$ can be written as

$$\mathbf{E}_i = \begin{pmatrix} E_{j,x} \\ 0 \\ E_{j,z} \end{pmatrix} e^{ik_x x - i\omega t} e^{ik_{j,z} z}, \quad j = 1, 2 \quad (12.11)$$

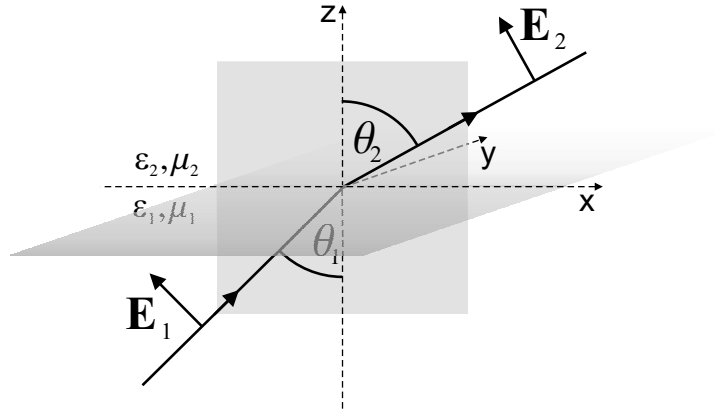


Figure 12.4: Interface between two media 1 and 2 with dielectric functions ε_1 and ε_2 . The interface is defined by $z=0$ in a Cartesian coordinate system. In each halfspace we consider only a single p-polarized wave because we are looking for homogeneous solutions that decay exponentially with distance from the interface.

The situation is depicted in Fig. 12.4. Since the wave vector parallel to the interface is conserved (see chapter 2) the following relations hold for the wave vector components

$$k_x^2 + k_{j,z}^2 = \varepsilon_j k^2, \quad j = 1, 2. \quad (12.12)$$

Here $k = 2\pi/\lambda$, where λ is the vacuum wavelength. Exploiting the fact that the displacement fields in both half spaces have to be source free, i.e. $\nabla \cdot \mathbf{D} = 0$, leads to

$$k_x E_{j,x} + k_{j,z} E_{j,z} = 0, \quad j = 1, 2, \quad (12.13)$$

which allows us to rewrite (12.11) as

$$\mathbf{E}_j = E_{j,x} \begin{pmatrix} 1 \\ 0 \\ -k_x/k_{j,z} \end{pmatrix} e^{ik_{j,z}z}, \quad j = 1, 2. \quad (12.14)$$

The factor $e^{ik_x x - i\omega t}$ is omitted to simplify the notation. Eq. (12.14) is particularly useful when a system of stratified layers is considered (see e.g. [8], p. 40 and problem 12.4). While (12.12) and (12.13) impose conditions that define the fields in the respective half spaces, we still have to match the fields at the interface using boundary conditions. Requiring continuity of the parallel component of \mathbf{E} and the perpendicular component of \mathbf{D} leads to another set of equations which read as

$$\begin{aligned} E_{1,x} - E_{2,x} &= 0 \\ \varepsilon_1 E_{1,z} - \varepsilon_2 E_{2,z} &= 0 \end{aligned} \quad (12.15)$$

Equations (12.13) and (12.15) form a homogeneous system of four equations for the four unknown field components. The existence of a solution requires that the respective determinant vanishes. This happens either for $k_x = 0$, which does surely not describe excitations that travel along the interface, or otherwise for

$$\varepsilon_1 k_{2,z} - \varepsilon_2 k_{1,z} = 0. \quad (12.16)$$

In combination with (12.12), Eq. (12.16) leads to a dispersion relation, i.e. a relation between the wave vector along the propagation direction and the angular frequency ω

$$k_x^2 = \frac{\varepsilon_1 \varepsilon_2}{\varepsilon_1 + \varepsilon_2} k^2 = \frac{\varepsilon_1 \varepsilon_2}{\varepsilon_1 + \varepsilon_2} \frac{\omega^2}{c^2}. \quad (12.17)$$

We also obtain an expression for the normal component of the wavevector

$$k_{j,z}^2 = \frac{\varepsilon_j^2}{\varepsilon_1 + \varepsilon_2} k^2, \quad j = 1, 2. \quad (12.18)$$

Having derived (12.17) and (12.18) we are in the position to discuss the conditions that have to be fulfilled for an interface mode to exist. For simplicity, we assume that

the imaginary parts of the complex dielectric functions are small compared with the real parts such that they may be neglected. A more detailed discussion that justifies this assumption will follow (see also [8]). We are looking for interface waves that propagate along the interface. This requires a real k_x .[†] Looking at (12.17) this can be fulfilled if both, the sum and the product of the dielectric functions are either both positive or both negative. In order to obtain a 'bound' solution, we require that the normal components of the wave vector are purely imaginary in both media giving rise to exponentially decaying solutions. This can only be achieved if the sum in the denominator of (12.18) is negative. From this we conclude that the conditions for an interface mode to exist are the following:

$$\varepsilon_1(\omega) \cdot \varepsilon_2(\omega) < 0 \quad (12.19)$$

$$\varepsilon_1(\omega) + \varepsilon_2(\omega) < 0 \quad (12.20)$$

which means that one of the dielectric functions must be negative with an absolute value exceeding that of the other. As we have seen in the previous section, metals, especially noble metals such as gold and silver, have a large negative real part of the dielectric constant along with a small imaginary part. Therefore, at the interface between a noble metal and a dielectric, such as glass or air, localized modes at the metal-dielectric interface can exist. Problem 12.3 discusses a possible solution for positive dielectric constants.

12.3.1 Properties of surface plasmon polaritons

Using the results of the previous section we will now discuss some properties of surface plasmon polaritons (SPP). To accommodate losses associated with electron scattering (ohmic losses) we have to consider the imaginary part of the metal's dielectric function [9]

$$\varepsilon_1 = \varepsilon'_1 + i\varepsilon''_1 \quad (12.21)$$

with ε'_1 and ε''_1 being real. We assume that the adjacent medium is a good dielectric with negligible losses, i.e. ε_2 is assumed to be real. We then naturally obtain a complex parallel wavenumber $k_x = k'_x + ik''_x$. The real part k'_x determines the SPP wavelength, while the imaginary part k''_x accounts for the damping of the SPP as it propagates along the interface. This is easy to see by using a complex k_x in (12.11). The real and imaginary parts of k_x can be determined from (12.17) under the assumption that $|\varepsilon''_1| \ll |\varepsilon'_1|$:

$$k'_x \approx \sqrt{\frac{\varepsilon'_1 \varepsilon_2}{\varepsilon'_1 + \varepsilon_2}} \frac{\omega}{c} \quad (12.22)$$

[†]Later we will see that by taking into account the imaginary parts of the dielectric functions k_x becomes complex which leads to a damped propagation in x direction.

$$k_x'' \approx \sqrt{\frac{\varepsilon_1' \varepsilon_2}{\varepsilon_1' + \varepsilon_2}} \frac{\varepsilon_1'' \varepsilon_2}{2\varepsilon_1'(\varepsilon_1' + \varepsilon_2)} \frac{\omega}{c} \quad (12.23)$$

in formal agreement with Eq. (12.17). For the SPP wavelength we thus obtain

$$\lambda_{\text{SPP}} = \frac{2\pi}{k_x'} \approx \sqrt{\frac{\varepsilon_1' + \varepsilon_2}{\varepsilon_1' \varepsilon_2}} \lambda \quad (12.24)$$

where λ is the wavelength of the excitation light in vacuum.

The propagation length of the SPP along the interface is determined by k_x'' which, according to (12.11), is responsible for an exponential damping of the electric field amplitude. The 1/e decay length of the electric field is $1/k_x''$ or $1/(2k_x'')$ for the intensity. This damping is caused by ohmic losses of the electrons participating in the SPP and finally results in a heating of the metal. Using $\varepsilon_2 = 1$ and the dielectric functions of silver ($\varepsilon_1 = -18.2 + 0.5i$) and gold ($\varepsilon_1 = -11.6 + 1.2i$) at a wavelength of 633 nm we obtain a 1/e intensity propagation lengths of the SPP of $\sim 60 \mu\text{m}$ and $\sim 10 \mu\text{m}$, respectively. The decay length of the SPP electric fields away from the interface can be obtained from (12.18) to first order in $|\varepsilon_1''|/|\varepsilon_1'|$ using (12.21) as

$$k_{1,z} = \frac{\omega}{c} \sqrt{\frac{\varepsilon_1'^2}{\varepsilon_1' + \varepsilon_2}} \left[1 + i \frac{\varepsilon_1''}{2\varepsilon_1'} \right] \quad (12.25)$$

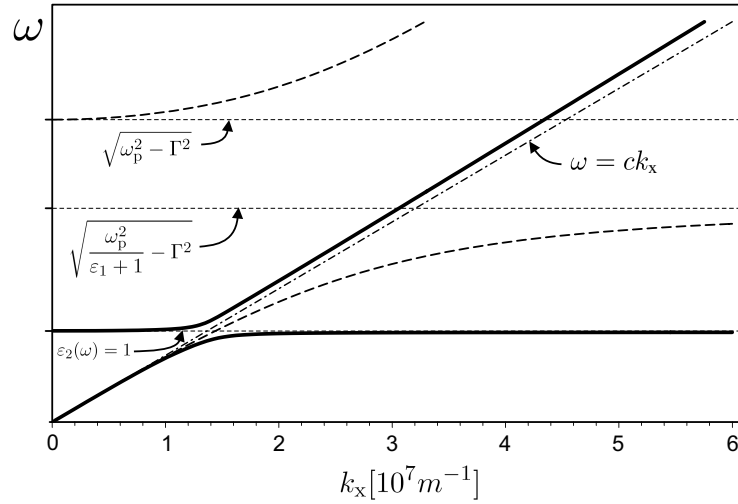


Figure 12.5: Dispersion relation of surface-plasmon polaritons at a gold/air interface. The solid line is the dispersion relation that results from a dielectric function accounting for a single interband transition. The dashed line results from using a Drude type dielectric function. The dash-dotted straight line is the light line $\omega = c \cdot k_x$ in air.

$$k_{2,z} = \frac{\omega}{c} \sqrt{\frac{\varepsilon_2^2}{\varepsilon_1' + \varepsilon_2}} \left[1 - i \frac{\varepsilon_1''}{2(\varepsilon_1' + \varepsilon_2)} \right] \quad (12.26)$$

Using the same parameters for silver and gold as before and safely neglecting the very small imaginary parts we obtain for the $1/e$ decay lengths pairs $(1/k_{1,z}, 1/k_{2,z})$ of the electric fields (23 nm, 421 nm) and (28 nm, 328 nm), respectively. This shows that the decay into the metal is much shorter than into the dielectric. It also shows that a sizable amount of the SPP electric field can reach through a thin enough metal film. It is now also clear that the conclusions made in section 12.3 based on ignoring the complex part of the dielectric function were correct. The decay of the SPP into the air halfspace was observed directly in [10] using a scanning tunnelling optical microscope.

An important parameter is the intensity enhancement near the interface due to the excitation of surface plasmons. This parameter can be obtained by evaluating the ratio of the incoming intensity and the intensity right above the metal interface. We skip this discussion for the moment and come back to this after the next section (see problem 12.4). However, we note that losses in the plasmon's propagation were directly derived from the metal's bulk dielectric function. This is a good approximation as long as the characteristic dimensions of the considered metal structures are larger than the electron mean-free path. If the dimensions become smaller, there is an increasing chance of electron scattering from the interface. In other words, close to the interface additional loss mechanisms have to be taken into account which locally increase the imaginary part of the metal's dielectric function. It is difficult to correctly account for these so-called nonlocal losses as the exact parameters are not known. Nevertheless, since the fields associated with surface plasmons penetrate into the metal by more than 10nm the nonlocal effects associated with the first few atomic layers can be safely ignored.

12.3.2 Excitation of surface plasmon polaritons

In order to excite surface-plasmon polaritons we have to fulfill both energy and momentum conservation. To see how this can be done we have to analyze the dispersion relation of the surface waves, i.e. the relation between energy in terms of the angular frequency ω and the momentum in terms of the wave vector in the propagation direction k_x given by Eq. (12.17) and Eq. (12.22). In order to plot this dispersion relation we assume that ε_1 is real, positive, and independent of ω which is true for e.g. air ($\varepsilon_1 = 1$).

For the metal we discuss two cases: (i) the pure Drude-Sommerfeld dielectric function given by (12.6) and (ii) the more realistic dielectric function that includes an interband transition (12.9). For both cases only the real part of $\varepsilon_2(\omega)$ is considered, neglecting the damping of the surface wave in the x -direction. Fig. 12.5 shows the

respective plots. The solid line is the dispersion relation for the more realistic metal. The thick dashed line is the corresponding dispersion relation when interband transition effects are neglected, i.e. for a pure Drude metal. The dash-dotted line is the light line $\omega = c \cdot k_x$ in air and the horizontal thin dashed lines mark important values of ω . For large k_x the simple Drude description results in a dispersion relation that clearly differs from the more realistic case, although the main features are similar. The dispersion relation shows two branches, a high energy and a low energy branch. The high energy branch, called Brewster mode, does not describe true surface waves since according to (12.18) the z -component of the wave vector in the metal is no longer purely imaginary. This branch will not be considered further. The low energy branch corresponds to a true interface wave, the surface plasmon polariton. The annex polariton is used to highlight the intimate coupling between the charge density wave on the metal surface (surface plasmon) with the light field in the dielectric medium (photon).

For completeness we need to mention that if damping is taken fully into account there is a continuous transition from the surface plasmon dispersion in Fig. 12.5 into

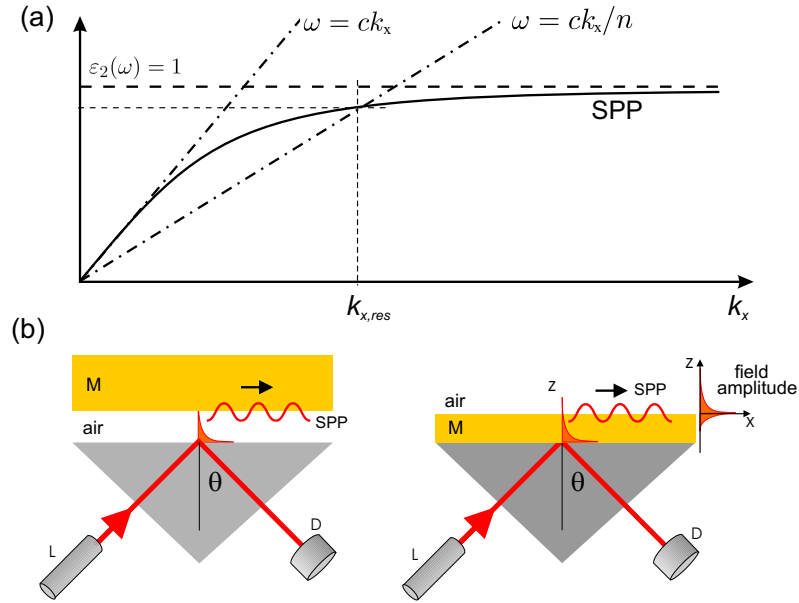


Figure 12.6: Excitation of surface plasmons. (a) Close up of the dispersion relation with the free-space light line and the tilted light line in glass. (b) Experimental arrangements to realize the condition sketched in (a). Left: Otto configuration. Right: Kretschmann configuration. The metal layer is sketched in yellow. L: laser, D: detector, M: metal layer.

the upper high energy branch. If we follow the dispersion curve in Fig. 12.5 starting from $\omega = 0$ then we first move continuously from the light line towards the horizontal line determined by the surface plasmon resonance condition $\varepsilon_2(\omega) = 1$. However, as the dispersion curve approaches this line the losses start to increase drastically. As a consequence, as ω is further increased the dispersion curve bends back and connects to the upper branch. In the connecting region the energy of the mode is strongly localized inside the metal which explains the high losses. The backbending effect has been experimentally verified (c.f. Ref. [11]) and poses a limit to the maximum wavenumber k_x that can be achieved in an experiment. Usually, this maximum k_x is smaller than $\approx 2\omega/c$.

An important feature of surface plasmons is that for a given energy $\hbar\omega$ the wave vector k_x is always larger than the wave vector of light in free space. This is obvious by inspecting (12.17) and also from Fig. 12.5 and Fig. 12.6 (a) where the light line ω/c is plotted as a dash-dotted line. This light line is asymptotically approached by the SPP dispersion for small energies. The physical reason for the increased momentum of the SPP is the strong coupling between light and surface charges. The light field has to "drag" the electrons along the metal surface. Consequently, this means that a SPP on a plane interface cannot be excited by light of any frequency that propagates in free space. Excitation of a SPP by light is only possible if the wavevector of the exciting light can be increased over its free-space value. There exist several ways to

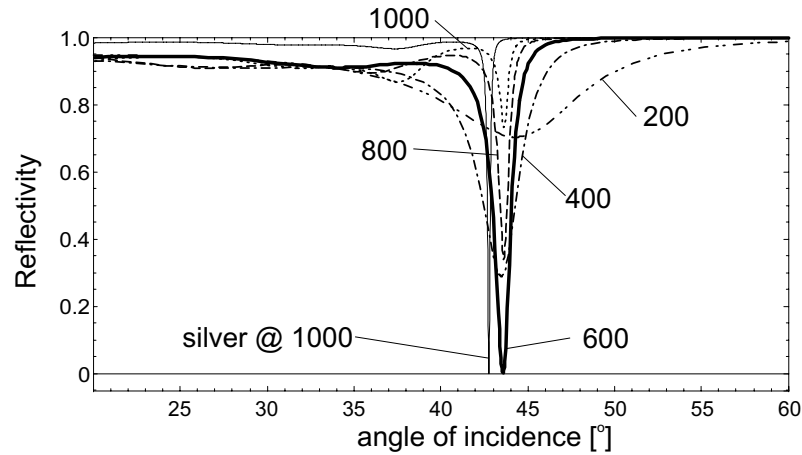


Figure 12.7: Excitation of surface plasmons in the Otto configuration. The reflectivity of the exciting beam is plotted as a function of the incident angle and for different air gaps (in nm). The curves are evaluated for a gold film. For comparison, a single trace is also plotted for silver for which the resonance is much sharper because of lower damping.

achieve this increase of the wave vector component. The conceptually most simple solution is to excite surface plasmons by means of evanescent waves created at the interface between a medium with refractive index $n > 1$. The light line in this case is tilted by a factor of n since $\omega = ck/n$. This situation is shown in Fig. 12.6 (a) which shows the SPP dispersion with the free-space light line and the tilted light line in glass.

Fig. 12.6 (b) shows a sketch of the possible experimental arrangements that realize this idea. In the Otto configuration [12] the tail of an evanescent wave at a glass/air interface is brought into contact with a metal-air interface that supports SPPs. For a sufficiently large separation between the two interfaces (gap width) the evanescent wave is only weakly influenced by the presence of the metal. By tuning the angle of incidence of the totally reflected beam inside the prism, the resonance condition for excitation of SPPs, i.e. the matching of the parallel wave vector component, can be fulfilled. The excitation of a SPP will show up as a minimum in the reflected light. The reflectivity of the system as a function of the angle of incidence and of the gap width is shown in Fig. 12.7. For the angle of incidence a clear resonance is observed at 43.5° . For a small gap width the resonance is broadened and shifted due to radiation damping of the SPP. This is caused by the presence of the glass halfspace which allows the SPP to rapidly decay radiatively by transforming the evanescent SPP field into a

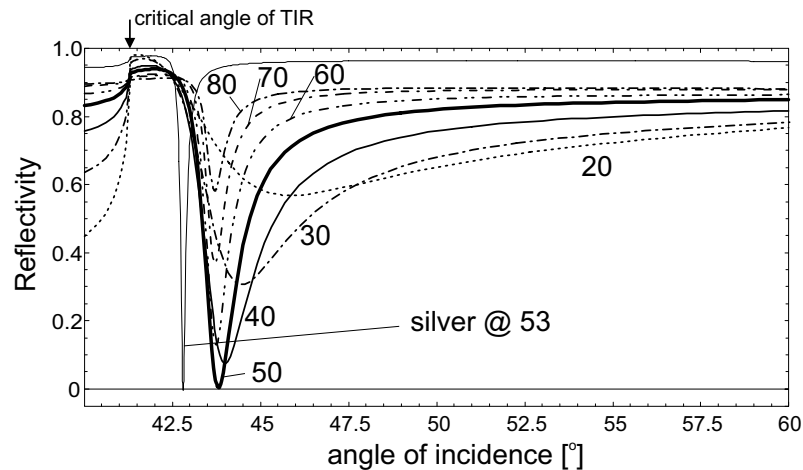


Figure 12.8: Excitation of surface plasmons in the Kretschmann configuration. The reflectivity of the exciting beam is plotted as a function of the incident angle and for different air gaps (in nm). The curves are evaluated for a gold film. For comparison a single trace is also plotted for silver. Note the the much sharper resonance due to the smaller damping of silver as compared to gold. The critical angle of total internal reflection shows up as a discontinuity marked by an arrow.

propagating field in the glass. On the other hand, for a gap width that is too large the SPP can no longer be efficiently excited and the resonance vanishes.

The Otto configuration proved to be experimentally inconvenient because of the challenging control of the tiny air gap between the two interfaces. In 1971 Kretschmann came up with an alternative method to excite SPP that solved this problem [13]. In his method, a thin metal film is deposited on top of a prism. The geometry is sketched in Fig. 12.6 (b). To excite a surface plasmon at the metal/air interface an evanescent wave created at the glass/metal interface has to penetrate through the metal layer. Here, similar arguments apply as for the Otto configuration. If the metal is too thin, the SPP will be strongly damped because of radiation damping into the glass. If the metal film is too thick the SPP can no longer be efficiently excited due to absorption in the metal. Fig. 12.8 shows the reflectivity of the excitation beam as a function of the metal film thickness and the angle of incidence. As before, the resonant excitation of surface plasmons is characterized by a dip in the reflectivity curves.

It is worth mentioning that for the occurrence of a minimum in the reflectivity curves in both the Otto and the Kretschmann configurations at least two (equivalent) physical interpretations can be given. The first interpretation is that the minimum can be thought of as being due to destructive interference between the totally reflected light and the light emitted by the SPP due to radiation damping. In the second interpretation, the missing light is assumed to have been totally converted to surface plasmons at the interface which carry away the energy along the interface such that it cannot reach the detector.

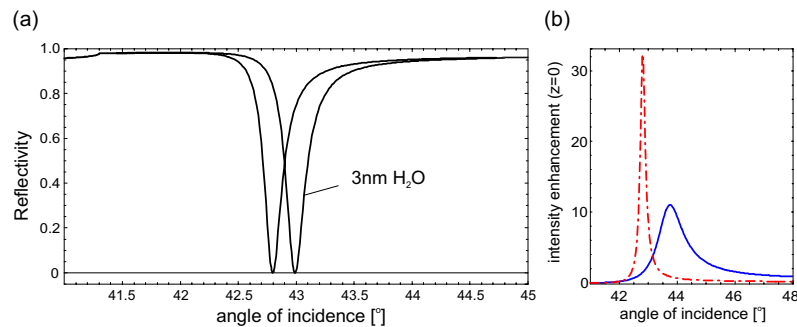


Figure 12.9: Surface plasmons used in sensor applications. (a) Calculated shift of the SPP resonance curve induced by a 3 nm layer of water ($n=1.33$) adsorbed on a 53 nm silver film. (b) Intensity enhancement near the metal surface as a function of the angle of incidence in the Kretschmann configuration. For silver ($\epsilon_1 = -18.2 + 0.5i$, dash-dotted line) and gold ($\epsilon_1 = -11.6 + 1.2i$, solid line) at a wavelength of 633 nm we observe a maximum intensity enhancement of ~ 32 and ~ 10 , respectively.

An alternative way to excite SPP is the use of a grating coupler [9]. Here, the increase of the wave vector necessary to match the SPP momentum is achieved by adding a reciprocal lattice vector of the grating to the free space wave vector. This requires in principle that the metal surface is structured with the right periodicity a over an extended spatial region. The new parallel wave vector then reads as $k'_x = k_x + 2\pi n/a$ with $2\pi n/a$ being a reciprocal lattice vector. A recent prominent application of this SPP excitation principle was used to enhance the interaction of subwavelength holes with SPP in silver films [14].

12.3.3 Surface plasmon sensors

The distinct resonance condition associated with the excitation of surface plasmons has found application in various sensor applications. For example, the position of the dip in the reflectivity curves can be used as an indicator for environmental changes. With this method, the adsorption or removal of target materials on the metal surface can be detected with submonolayer accuracy. Fig. 12.9 illustrates this capability by a simulation. It shows the effect of a 3 nm layer of water on top of a 53 nm thick silver film on glass. A strongly shifted plasmon resonance curve can be observed. Assuming that the angle of incidence of the excitation beam has been adjusted to the dip in the reflectivity curve, the deposition of a minute amount of material increases the signal (reflectivity) drastically. This means that the full dynamic range of a low-noise intensity measurement can be used to measure a coverage ranging between 0 and 3 nm. Consequently, SPP sensors are very attractive for applications ranging from biological binding assays to environmental sensing. For reviews see e.g. [15, 16].

The reason for the extreme sensitivity lies in the fact that the light intensity near the metal surface is strongly enhanced. In the Kretschmann configuration, this enhancement factor can be determined by evaluating the ratio of the intensity above the metal and the incoming intensity. In Fig. 12.9 (b) this ratio is calculated and plotted as a function of the angle of incidence for both gold and silver for a 50 nm thin film. A clear resonant behavior is again observed which reflects the presence of the SPP.

12.4 Surface plasmons in nano-optics

Scanning near-field optical microscopy as well as fluorescence studies lead to new ways of exciting SPP [17, 20, 19]. The parallel components of the wavevector (k_x) necessary for SPP excitation are also present in subwavelength confined optical near fields in the vicinity of subwavelength apertures, metallic particles or even fluorescent molecules. If such confined fields are brought close enough to a suitable interface,

coupling to SPP can be accomplished *locally*. Fig. 12.10 shows the principal arrangements. A metal film resides on a (hemispherical) glass prism to allow light (e.g. due to radiation damping of the SPP) to escape and to be recorded. In order to excite surface plasmons, the exciting light field needs to have evanescent field components that match the parallel wavevector k_x of the surface plasmon. As an illustration, Fig. 12.11 (a) shows the excitation of surface plasmons with an oscillating dipole placed near the surface of a thin silver film deposited on a glass surface. The figure depicts contourlines of constant power density evaluated at a certain instant of time and displayed on a logarithmic scale. The surface plasmons propagating on the top surface decay radiatively as seen by the wavefronts in the lower medium. The situation is reciprocal to the situation of the Kretschmann configuration discussed earlier where such radiation is used to excite surface plasmons. Also seen in Fig. 12.11 (a) is the excitation of surface plasmons at the metal-glass interface. However, at the wavelength of $\lambda = 370\text{nm}$, these plasmons are strongly damped and therefore do not propagate long distance. Fig. 12.11 (b) shows the radiation pattern evaluated in the lower medium (glass). It corresponds to the radiation collected with a high numerical aperture lens and then projected on a photographic plate. The circle in the center indicates the critical angle of total internal reflection of an air-glass interface $\theta_c = \arcsin(1/n)$, with n being the index of refraction of glass. Obviously, the plasmon radiates into an angle beyond θ_c . In fact, the emission angle corresponds to the Kretschmann angle discussed previously (c.f. Fig. 12.8). Surface plasmons can only be excited with p-polarized field components as there needs to be a driving force on the free charges towards the interface. This is the reason why the radiation pattern shows up as two lobes.

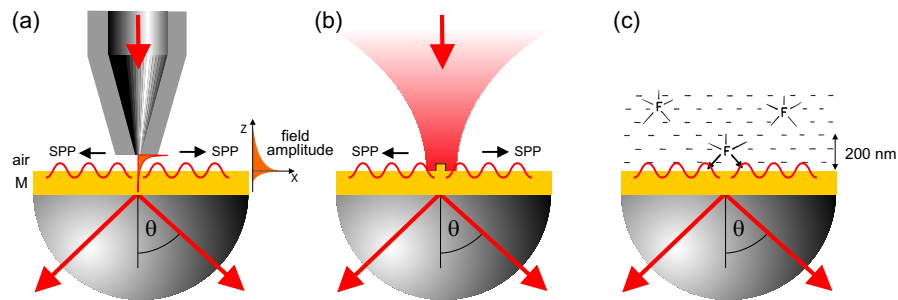


Figure 12.10: Local excitation of surface plasmons on a metal film with different confined light fields. (a) a subwavelength light source such as an aperture probe [17], (b) an irradiated nanoparticle [18], and (c) fluorescent molecules [19]. In all cases, surface plasmons are excited by evanescent field components that match the parallel wavevector k_x of the surface plasmon.

The dipole is an ideal excitation source and more realistic sources used in practice have finite dimensions. The size of the source and its proximity to the metal surface determines the spatial spectrum that is available for the excitation of surface plasmons. If the source is too far from the metal surface only plane wave components of the angular spectrum reach the metal surface and hence coupling to surface plasmons is inhibited. Fig. 12.12 (a) shows a sketch of the spatial spectrum (spatial Fourier transform) of a confined light source evaluated in planes at different distances from the source (see inset). The spectrum is broad close to the source but narrows with increasing distance from the source. The same figure also shows the spatial spectrum of a surface plasmon supported by a silver film. The excitation of the surface plasmon is possible because of the overlap of the spatial spectrum of source and surface plasmon. Due to the decrease in field confinement for increasing distance from the source, a characteristic distance dependence for the surface plasmon excitation efficiency is expected. As discussed before, in a thin film configuration, surface plasmon excitation can be monitored by observing the plasmon's leakage radiation into the glass half space. Fig. 12.12 (b) shows, for a thin gold and silver film deposited on a glass hemisphere, the total intensity of surface plasmon leakage radiation as a function of the distance between source (aperture) and the metal surface. The curve

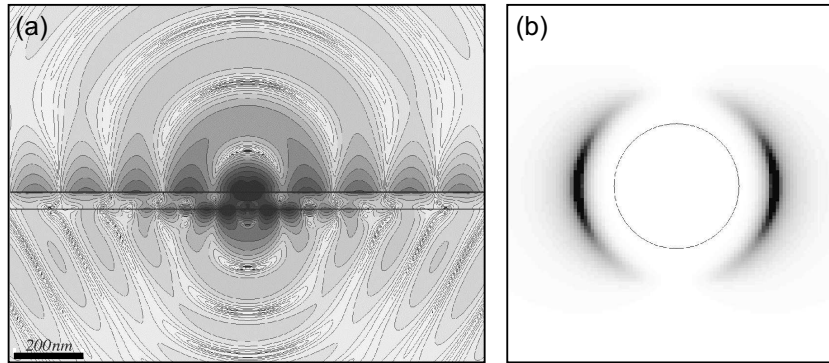


Figure 12.11: Excitation of surface plasmons with a dipole source placed 5nm above a 50nm silver layer supported by a glass substrate. The excitation wavelength is $\lambda = 370nm$ and the dipole moment is parallel to the interface. (a) Lines of constant power density (factor of 2 between successive contour lines) depicted at a certain instant of time. The figure shows the surface plasmon propagation along the top surface of the silver film and also the radiative decay into the lower half space. (b) Radiation pattern evaluated on a horizontal plane in the lower medium. The circle indicates the critical angle of total internal reflection at an air-glass interface. The two lobes result from the radiative decay of surface plasmons excited by the dipole source.

labeled 'MMP' indicates a numerical simulation. All curves clearly show a dip for very small distances. This dip is likely due to the perturbation of the surface plasmon resonance condition by the proximity of the probe, i.e. the coupling between probe and sample (see also Fig. 12.7 as an illustration of this effect). For a source with vanishing dimensions (a dipole) no such dip is observed.

The leakage radiation can also be used to visualize the propagation length of surface plasmons. This is done by imaging the metal/glass interface onto a camera using a high NA microscope objective that can capture the leakage radiation above the critical angle (see Fig. 12.12 c). The extension of the SPP propagation is in good agreement with Eq. (12.17). The effect of a changing gap width and the effect of changing the polarization can be used to control the intensity and the direction in which surface plasmons are launched. While the excitation of surface plasmons in Fig. 12.12 has been accomplished with a near-field aperture probe, the example in Fig. 12.13 shows the same experiment but with a laser-irradiated nanoparticle acting as excitation source. In this experiment, the surface plasmon propagation is visualized by the fluorescence intensity of a thin layer of fluorophores deposited on the metal surface. A double-lobed emission pattern is observed due to the fact that surface plasmons can only be excited by p-polarized field components of the near-field. Control over the direction of emission is possible via the choice of the polarization of the excitation beam [20].

The coupling of fluorophores to surface plasmons can drastically improve the sen-

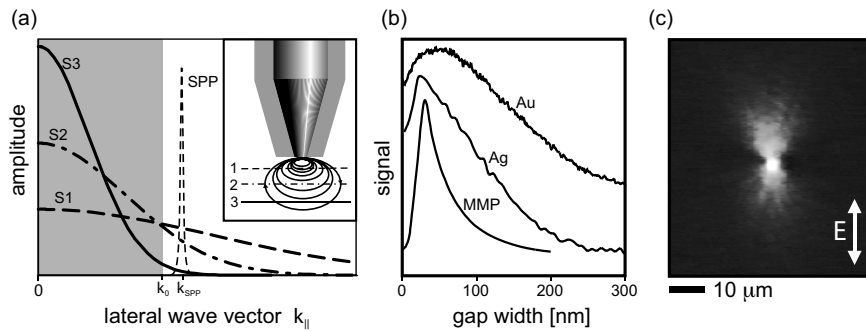


Figure 12.12: Local excitation of surface plasmons with a near-field aperture probe. (a) Sketch of the overlap of the spatial spectra of source (evaluated in planes at different distances from the source) and the surface plasmon on a silver film. (b) Distance-dependence of the coupling. The dip at short distances is a result of probe-sample coupling, i.e. the presence of the probe locally modifies the plasmon resonance condition. (c) Image of plasmon propagation recorded by focusing the leakage radiation on an image plane.

sitivity of fluorescence-based assays in medical diagnostics, biotechnology and gene expression. For finite distances between metal and fluorophores (<200 nm) the coupling to surface plasmons leads to strong fluorescence signal enhancement and high directionality of the emission. For example, an immunoassay for the detection of the cardiac marker myoglobin has been developed in Ref. [22]. An interplay between surface plasmons launched by an aperture probe and surface plasmons excited by particle scattering has been studied in Ref. [17]. Fig. 12.14 shows experimentally recorded surface plasmon interference patterns on a smooth silver film with some irregularities. The periodicity of the fringes of 240 ± 5 nm is exactly half the surface plasmon wavelength. The contrast in this image is obtained by recording the intensity of the leakage radiation as the aperture probe is raster scanned over the sample surface. Thus, the fringes are due to surface plasmon standing waves that build up between the probe and the irregularities that act as scattering centers. Strongest leakage radiation is obtained for probe-scatterer distances that are integer multiples of half the surface plasmon wavelength.

The observation that surface plasmons originating from different scattering centers on a surface can interfere, suggests the possibility of building optical elements for surface plasmon nano-optics [23-25]. Today the field of 'plasmonics' covers such research activities. Of particular interest in this context is the development of plasmon-based waveguiding structures that allow for transport and manipulation of light at sub-wavelength scales. Several recent experiments have demonstrated the use of surface

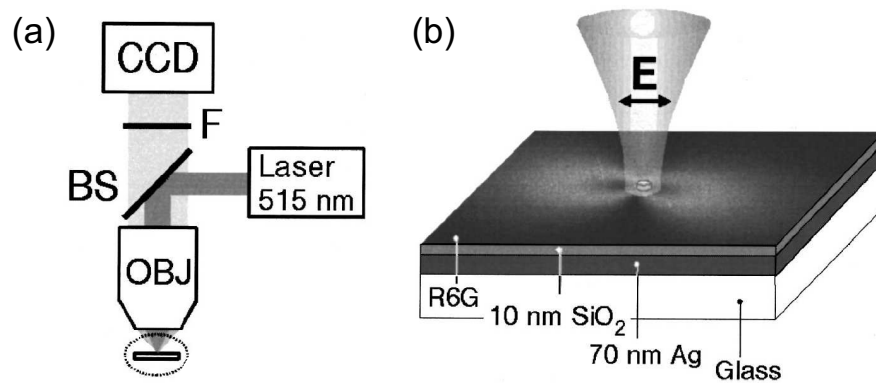


Figure 12.13: Excitation of surface plasmons by a subwavelength-scale protrusion located on the top surface of a metal film. (a) Setup, (b) Close up of the particle-beam interaction area. In this experiment, the surface plasmons are detected by the fluorescence intensity of a thin layer of fluorescent molecules deposited on a dielectric spacer layer. From [20].

plasmons in waveguiding applications [26]. To measure the intrinsic damping of the waveguides, radiation losses have to be eliminated which is accomplished by preparing the waveguide using a sandwich structure of glass, aluminum, SiO_2 , and gold [26]. As an example, Fig. 12.15(a) shows a near-field measurement of a surface plasmon waveguide recorded by photon scanning tunneling microscopy (PSTM) (see chapter 5). Surface plasmon reflection at the end of the waveguide leads to a standing wave pattern which can be evaluated to measure e.g. the surface plasmon wavelength. The figure demonstrates that surface plasmon propagation can extend over several μm underlining their potential use in future subwavelength integrated optical devices. For comparison, Fig. 12.15(b) shows the results of a simulation for an even thinner waveguide [27]. Similar qualitative features are observed.

12.4.1 Plasmons supported by wires and particles

For surface plasmon polaritons propagating on plane interfaces we observed that the electromagnetic field is strongly localized in one dimension, i.e. normal to the interface. In the context of nano-optics we are also interested in establishing field confinement in two or even three dimensions. Therefore it is useful to theoretically analyze the

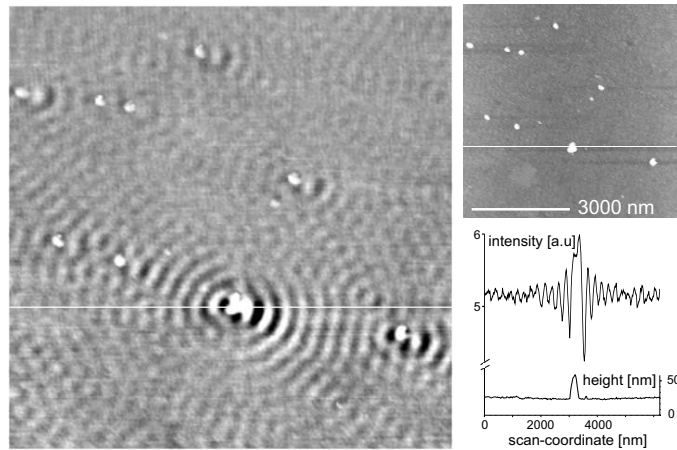


Figure 12.14: Interference of locally excited surface plasmons. Right panel: Integrated leakage radiation from a silver film with some protrusions recorded as an aperture probe is raster-scanned over the sample surface. The fringes correspond to surface plasmon standing wave patterns that build up between the protrusions and the aperture probe. Left panel: Shear-force topography of the area shown in the optical image and line cuts along the white line through both, topography and optical image.

electromagnetic modes associated with thin wires and small particles. In order to keep the analysis simple, we will limit the discussion to the quasi-static approximation which neglects retardation. Thus, it is assumed that all points of an object respond simultaneously to an incoming (excitation) field. This is only true if the characteristic size of the object is much smaller than the wavelength of light. In the quasi-static approximation the Helmholtz equation reduces to the Laplace equation which is much easier to solve. A detailed discussion can be found e.g. in [28]. The solutions that are obtained here are the quasi-static near-fields and scattering cross-sections of the considered objects. For example, the electric field of an oscillating dipole

$$\mathbf{E}(r\mathbf{n}, t) = \frac{1}{4\pi\epsilon_0} \left[k^2(\mathbf{n} \times \boldsymbol{\mu}) \times \mathbf{n} \frac{e^{ikr}}{r} + [3\mathbf{n}(\mathbf{n} \cdot \boldsymbol{\mu}) - \boldsymbol{\mu}] \left(\frac{1}{r^3} - \frac{ik}{r^2} \right) e^{ikr} \right] e^{i\omega t} \quad (12.27)$$

with $\boldsymbol{\mu}$ denoting the dipole moment, can be approximated in the near-field zone $kr \ll 1$ as

$$\mathbf{E}(r\mathbf{n}, t) = \frac{1}{4\pi\epsilon_0} [3\mathbf{n}(\mathbf{n} \cdot \mathbf{p}) - \mathbf{p}] \frac{e^{i\omega t}}{r^3} \quad (12.28)$$

which is exactly the electrostatic field of a point dipole, only that it oscillates in time with $e^{i\omega t}$, which is the reason why it is termed *quasi*-static. In the quasi-static limit the electric field can be represented by a potential as $\mathbf{E} = -\nabla\Phi$. The potential has

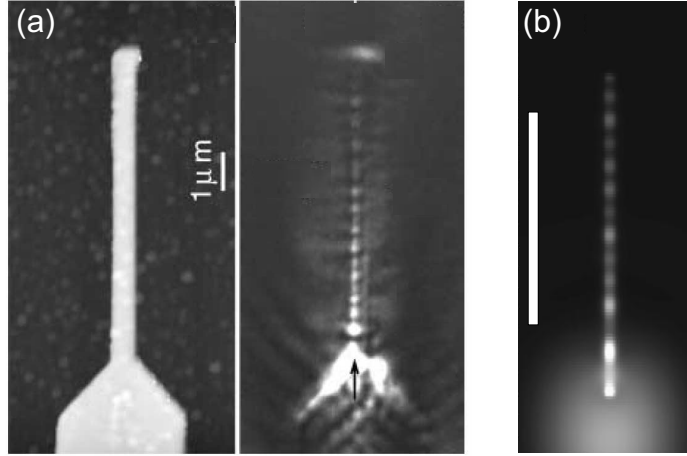


Figure 12.15: SPP waveguides. (a) Propagation, reflection and interference of surface plasmons guided by a gold nanowire with a width of $\lambda/4$ with $\lambda=800$ nm. Left: shear-force topography, right: optical image recorded with a photon scanning tunneling microscope (PSTM). From [26] without permission. (b) Simulation of surface plasmon propagation on a finite length gold rod showing a similar standing wave pattern. Scale bar $1 \mu\text{m}$. From [27] without permission.

to satisfy the Laplace equation

$$\nabla^2 \Phi = 0 \quad (12.29)$$

and the boundary conditions between adjacent materials (see chapter 2). In the following we will analyze the solutions of (12.29) for a thin metal wire and a small metal particle, respectively.

Plasmon resonance of a thin wire

Let us consider a thin cylindrical wire with radius a centered at the origin and extending along the z -axis to infinity. The wire is illuminated by an x -polarized plane wave. The geometry is sketched in Fig. 12.17. To tackle this problem we introduce cylindrical coordinates

$$\begin{aligned} x &= \rho \cos \varphi \\ y &= \rho \sin \varphi \\ z &= z \end{aligned} \quad (12.30)$$

and express the Laplace equation in a cylindrical coordinate system as

$$\frac{1}{\rho} \frac{\partial}{\partial \rho} \left(\rho \frac{\partial \Phi}{\partial \rho} \right) + \frac{1}{\rho^2} \left(\frac{\partial^2 \Phi}{\partial \varphi^2} \right) = 0 . \quad (12.31)$$

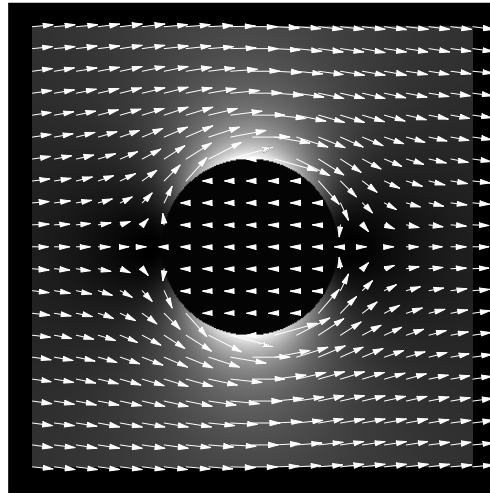


Figure 12.16: Near-field distribution around a gold wire in the quasi-static limit at a wavelength of 633 nm.

Here, we have accounted for the fact that there is no z -dependence. The Laplace equation (12.31) can be separated using the Ansatz $\Phi(\rho, \varphi) = R(\rho)\Theta(\varphi)$ yielding

$$\frac{1}{R} \left(\rho \frac{\partial}{\partial \rho} \left(\rho \frac{\partial R}{\partial \rho} \right) \right) = -\frac{1}{\Theta} \left(\frac{\partial^2 \Theta}{\partial \varphi^2} \right) \equiv m^2. \quad (12.32)$$

The angular part has solutions of the form

$$\Theta(\varphi) = c_1 \cos(m\varphi) + c_2 \sin(m\varphi) \quad (12.33)$$

which implies for the present problem that m must be an integer to ensure the 2π periodicity of the solution. The radial part has solutions of the form

$$\begin{aligned} R(\rho) &= c_3 \rho^m + c_4 \rho^{-m}, & m > 0 \\ R(\rho) &= c_3 \ln \rho + c_4, & m = 0 \end{aligned} \quad (12.34)$$

with the same m as introduced in (12.32). Because of the symmetry imposed by the polarization of the exciting electric field (x -axis) only $\cos(m\varphi)$ terms need to be considered. Furthermore, the \ln solution for $m = 0$ in (12.34) has to be rejected because it leads to a diverging field at the origin and at infinity. We therefore use the following expansion

$$\begin{aligned} \Phi(\rho < a) &= \Phi_1 = \sum_{n=1}^{\infty} \alpha_n \rho^n \cos(n\varphi), \\ \Phi(\rho > a) &= \Phi_2 = \Phi_{\text{scatter}} + \Phi_0 = \sum_{n=1}^{\infty} \beta_n \rho^{-n} \cos(n\varphi) - E_0 \rho \cos(\varphi) \end{aligned} \quad (12.35)$$

where α_n and β_n are constants to be determined from the boundary conditions on the wire surface $\rho = a$. In terms of the potential Φ the boundary conditions read as

$$\begin{aligned} \left[\frac{\partial \Phi_1}{\partial \varphi} \right]_{\rho=a} &= \left[\frac{\partial \Phi_2}{\partial \varphi} \right]_{\rho=a} \\ \varepsilon_1 \left[\frac{\partial \Phi_1}{\partial \rho} \right]_{\rho=a} &= \varepsilon_2 \left[\frac{\partial \Phi_2}{\partial \rho} \right]_{\rho=a} \end{aligned} \quad (12.36)$$

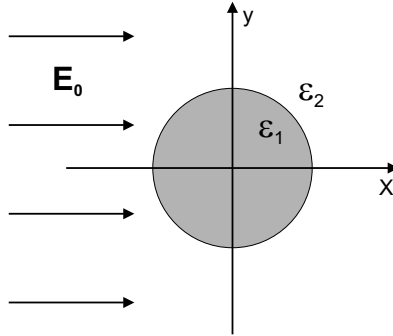


Figure 12.17: Cut through a thin wire that is illuminated by an x -polarized plane wave.

which follows from the continuity requirement for the tangential component of the electric field and the normal component of the electric displacement. Here, ε_1 and ε_2 are the complex dielectric constants of the wire and the surrounding, respectively. In order to evaluate (12.36) we use the fact that the functions $\cos(n\varphi)$ are orthogonal. Introducing (12.35) into (12.36) we immediately see that α_n and β_n vanish for $n > 1$. For $n = 1$ we obtain

$$\alpha_1 = -E_0 \frac{2\varepsilon_2}{\varepsilon_1 + \varepsilon_2}, \quad \beta_1 = a^2 E_0 \frac{\varepsilon_1 - \varepsilon_2}{\varepsilon_1 + \varepsilon_2}. \quad (12.37)$$

With these coefficients the solution for the electric field turns out to be

$$\mathbf{E}_1 = E_0 \frac{2\varepsilon_2}{\varepsilon_1 + \varepsilon_2} \mathbf{e}_x \quad (12.38)$$

$$\mathbf{E}_2 = E_0 \mathbf{e}_x + E_0 \frac{\varepsilon_1 - \varepsilon_2}{\varepsilon_1 + \varepsilon_2} \frac{a^2}{\rho^2} (1 - 2 \sin^2 \varphi) \mathbf{e}_x + 2E_0 \frac{\varepsilon_1 - \varepsilon_2}{\varepsilon_1 + \varepsilon_2} a^2 \sin \varphi \cos \varphi \mathbf{e}_y \quad (12.39)$$

where we re-introduced Cartesian coordinates.

In most applications the dispersion (frequency dependence) of the dielectric medium surrounding the metal can be ignored and one can assume a constant ε_2 . On the other hand, the metal's dielectric function is strongly wavelength dependent. The solution for the fields is characterized by the denominator $\varepsilon_1 + \varepsilon_2$. Consequently, the fields diverge when $\varepsilon_1(\lambda) = -\text{Re}(\varepsilon_2)$. This is the resonance condition for a collective electron oscillation in a wire that is excited by an electric field polarized perpendicular to the wire axis. The shape of the resonance is determined by the dielectric function $\varepsilon_1(\lambda)$. Similar to the case of the plane interface discussed earlier, changes in the dielectric constant of the surrounding medium (ε_2) lead to shifts of the resonance (see below). Notice, that no resonances exist if the electric field is polarized along the wire axis. As in the plane interface case, the excitation of surface plasmons relies on a surface charge accumulation at the surface of the wire. In order to drive the charges to the interface the electric field needs to have a polarization component normal to the metal surface.

To understand surface plasmon propagation *along* a cylindrical wire one needs to solve the full vector wave equation. Such an analysis has been done in Ref. [30] for solid metal wires and for hollow metal wires. An interesting outcome of this study is that energy can be coupled adiabatically from guided modes propagating inside a hollow metal waveguide to surface modes propagating on the outside of the waveguide. The propagation along the wire axis z is determined by the factor

$$\exp[i(k_z z - \omega t)], \quad (12.40)$$

where $k_z = \beta + i\alpha$ is the complex propagation constant. β and α are designated as phase constant and attenuation constant, respectively. For the two best propagating

surface modes, Fig. 12.18 a) shows the propagation constant of an aluminum cylinder as a function of the cylinder radius a . The TM_0 mode exhibits a radial polarization, i.e. the electrical field is axially symmetric. On the other hand, the HE_1 mode has a $\cos\varphi$ angular dependence and, as the radius a tends to zero, it converts to an unattenuated plane wave ($k_z \approx \omega/c$) that is infinitely extended. The situation is different for the TM_0 mode. As the radius a is decreased, its phase constant β becomes larger and the transverse field distribution becomes better localized. However, also the attenuation constant α increases and hence for too thin wires the surface plasmon propagation length becomes very small. Recently, it has been pointed out that both the phase velocity and the group velocity of the TM_0 mode tend to zero as the diameter a is decreased [31]. Therefore, a pulse propagating along a wire whose diameter is adiabatically thinned down never reaches the end of the wire, i.e. it's tip. Notice, that modes propagating on the surface of a metal wire have already been characterized in 1909 [32]. It was realized that single wires can transport energy almost free of losses but at the expense of having poor localization, i.e. the fields extend in the surrounding medium over very large distances. Therefore, transmission lines consist of two or more wires.

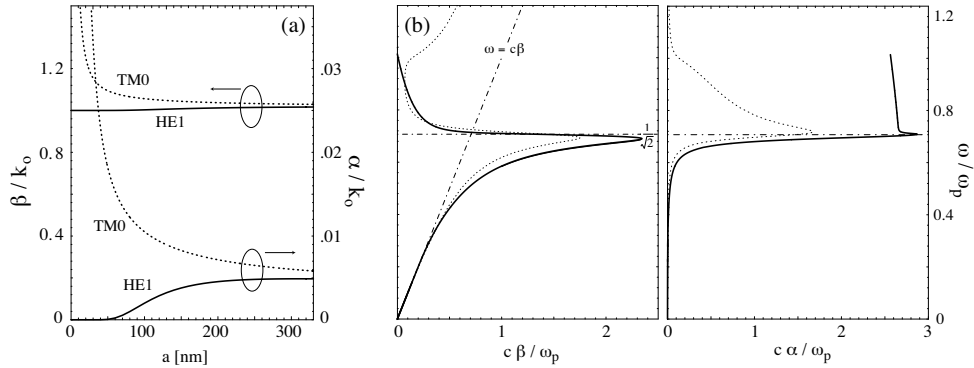


Figure 12.18: (a) Propagation constant $k_z = \beta + i\alpha$ of the two lowest surface modes supported by an aluminum wire at a wavelength of $\lambda = 488$ nm. a denotes the wire diameter and $k_0 = \omega/c$. (b) Frequency dispersion of the HE_1 surface mode of a $a = 50$ nm aluminum wire. ω_p denotes the plasma frequency of aluminum. The dotted line indicates the corresponding dispersion on a plane interface. Notice the backbending effect discussed earlier.

Plasmon resonance of a small spherical particle

The plasmon resonance for a small spherical particle of radius a in the electrostatic limit can be found in much a similar way as for the thin wire. Here, we have to express the Laplace equation (12.29) in spherical coordinates (r, θ, φ) as

$$\frac{1}{r^2 \sin \theta} \left[\sin \theta \frac{\partial}{\partial r} \left(r^2 \frac{\partial}{\partial r} \right) + \frac{\partial}{\partial \theta} \left(\sin \theta \frac{\partial}{\partial \theta} \right) + \frac{1}{\sin \theta} \frac{\partial^2}{\partial \varphi^2} \right] \Phi(r, \theta, \varphi) = 0 \quad (12.41)$$

The solutions are of the form

$$\Phi(r, \theta, \varphi) = \sum_{l,m} b_{l,m} \cdot \Phi_{l,m}(r, \theta, \varphi) \quad (12.42)$$

Here, the $b_{l,m}$ are constant coefficients to be determined from the boundary conditions and the $\Phi_{l,m}$ are of the form

$$\Phi_{l,m} = \begin{Bmatrix} r^l \\ r^{-l-1} \end{Bmatrix} \begin{Bmatrix} P_l^m(\cos \theta) \\ Q_l^m(\cos \theta) \end{Bmatrix} \begin{Bmatrix} e^{im\varphi} \\ e^{-im\varphi} \end{Bmatrix} \quad (12.43)$$

where the $P_l^m(\cos \theta)$ are the associated Legendre functions and the $Q_l^m(\cos \theta)$ are the Legendre functions of the second kind [29]. Linear combinations of the functions in the upper and the lower row of (12.43) may have to be chosen according to the particular problem to avoid infinities at the origin or at infinite distance. Again, the continuity of the tangential electric fields and the normal components of the electric displacements at the surface of the sphere imply that

$$\begin{aligned} \left[\frac{\partial \Phi_1}{\partial \theta} \right]_{r=a} &= \left[\frac{\partial \Phi_2}{\partial \theta} \right]_{r=a} \\ \varepsilon_1 \left[\frac{\partial \Phi_1}{\partial r} \right]_{r=a} &= \varepsilon_2 \left[\frac{\partial \Phi_2}{\partial r} \right]_{r=a} \end{aligned} \quad (12.44)$$

Here, Φ_1 is the potential inside the sphere and $\Phi_2 = \Phi_{\text{scatter}} + \Phi_0$ is the potential outside the sphere consisting again of the potentials of the incoming and the scattered fields. For the incoming electric field we assume, as for the case of the wire, that it is homogeneous and directed along the x-direction. Consequently, $\Phi_0 = -E_0 x = -E_0 r P_1^0(\cos(\theta))$. Evaluation of the boundary conditions leads to

$$\begin{aligned} \Phi_1 &= -E_0 \frac{3\varepsilon_2}{\varepsilon_1 + 2\varepsilon_2} r \cos \theta \\ \Phi_2 &= -E_0 r \cos \theta + E_0 \frac{\varepsilon_1 - \varepsilon_2}{\varepsilon_1 + 2\varepsilon_2} a^3 \frac{\cos \theta}{r^2} \end{aligned} \quad (12.45)$$

(see problem 12.7 and e.g. [4]). The most important difference to the solution for the wire is the distance dependence $1/r^2$ as compared to $1/r$ and the modified resonance condition with ε_2 multiplied by a factor of 2 in the denominator. It is also important to note, that the field is independent of the azimuth angle φ , which is a result of the

symmetry implied by the direction of the applied electric field. Finally, the electric field can be calculated from (12.45) using $\mathbf{E} = -\nabla\Phi$ and turns out to be

$$\mathbf{E}_1 = E_0 \frac{3\varepsilon_2}{\varepsilon_1 + 2\varepsilon_2} (\cos\theta \mathbf{e}_r - \sin\theta \mathbf{e}_\theta) = E_0 \frac{3\varepsilon_2}{\varepsilon_1 + 2\varepsilon_2} \mathbf{e}_x \quad (12.46)$$

$$\mathbf{E}_2 = E_0 (\cos\theta \mathbf{e}_r - \sin\theta \mathbf{e}_\theta) + \frac{\varepsilon_1 - \varepsilon_2}{\varepsilon_1 + 2\varepsilon_2} \frac{a^3}{r^3} E_0 (2\cos\theta \mathbf{e}_r + \sin\theta \mathbf{e}_\theta) . \quad (12.47)$$

The field distribution near a resonant gold or silver nanoparticle looks qualitatively similar as the plot shown in Fig. 12.16 for the case of the thin wire. On resonance the field is strongly localized near the surface of the particle. An interesting feature is that the electric field inside the particle is homogeneous. For metal particles this is an unexpected result as we know that electromagnetic fields decay exponentially into metals. Consequently, the quasi-static approximation is only valid for particles that are smaller in size than the skin depth d of the metal ($d = \lambda/[4\pi\sqrt{\varepsilon}]$). Another important finding is that the scattered field [second term in (12.47)] is identical to the electrostatic field of a dipole $\boldsymbol{\mu}$ located at the center of the sphere. The dipole is induced by the external field \mathbf{E}_0 and has the value $\boldsymbol{\mu} = \varepsilon_2\alpha(\omega)\mathbf{E}_0$, with α denoting the polarizability[‡]

$$\alpha(\omega) = 4\pi\varepsilon_o a^3 \frac{\varepsilon_1(\omega) - \varepsilon_2}{\varepsilon_1(\omega) + 2\varepsilon_2} . \quad (12.48)$$

This relationship can be easily verified by comparison with Eq. (12.28). The scattering cross-section of the sphere is then obtained by dividing the total radiated power of the sphere's dipole (see e.g. chapter 8) by the energy density of the exciting plane wave. This results in

$$\sigma_{\text{scatt}} = \frac{k^4}{6\pi\varepsilon_o^2} |\alpha(\omega)|^2 , \quad (12.49)$$

with k being the wavevector in the surrounding medium. Notice that the polarizability (12.48) violates the optical theorem in the dipole limit, i.e. scattering is not accounted for. This inconsistency can be corrected by allowing the particle to interact with itself (radiation reaction). As discussed in problem 8.5, the inclusion of radiation reaction introduces an additional term to (12.48). See also problem 15.4.

Fig. 12.19 shows plots of the normalized scattering cross-section of 20 nm radius gold and silver particles in different media. Note that the resonance for the silver particles is in the ultraviolet spectral range while for gold the maximum scattering occurs around 530 nm. A redshift of the resonance is observed if the dielectric constant of the environment is increased.

[‡]Notice, that we use dimensionless (relative) dielectric constants, i.e. the vacuum permeability ε_o is *not* contained in ε_2 .

The power removed from the incident beam due to the presence of a particle is not only due to scattering but also due to absorption. The sum of absorption and scattering is called *extinction*. Therefore, we also need to calculate the power that is dissipated inside the particle. Using Poynting's theorem we know that the dissipated power by a point dipole is determined as $P_{abs} = (\omega/2) \text{Im} [\boldsymbol{\mu} \cdot \mathbf{E}_0^*]$. Using $\boldsymbol{\mu} = \varepsilon_2 \alpha \mathbf{E}_0$, with ε_2 being real, and the expression for the intensity of the exciting plane wave in the surrounding medium, we find for the absorption cross-section

$$\sigma_{abs} = \frac{k}{\varepsilon_o} \text{Im} [\alpha(\omega)] . \quad (12.50)$$

Again, k is the wavevector in the surrounding medium. It turns out that σ_{abs} scales with a^3 whereas σ_{scatt} scales with a^6 . Consequently, for large particles extinction is dominated by scattering whereas for small particles it is associated with absorption. This effect can be used to detect extremely small metal particles down to 2.5 nm diameter which are used as labels in biological samples [33]. The transition between the two size regimes is characterized by a distinct color change. For example, small gold particles absorb green and blue light and thus render a red color. On the other hand, larger gold particles scatter predominantly in the green and hence render a

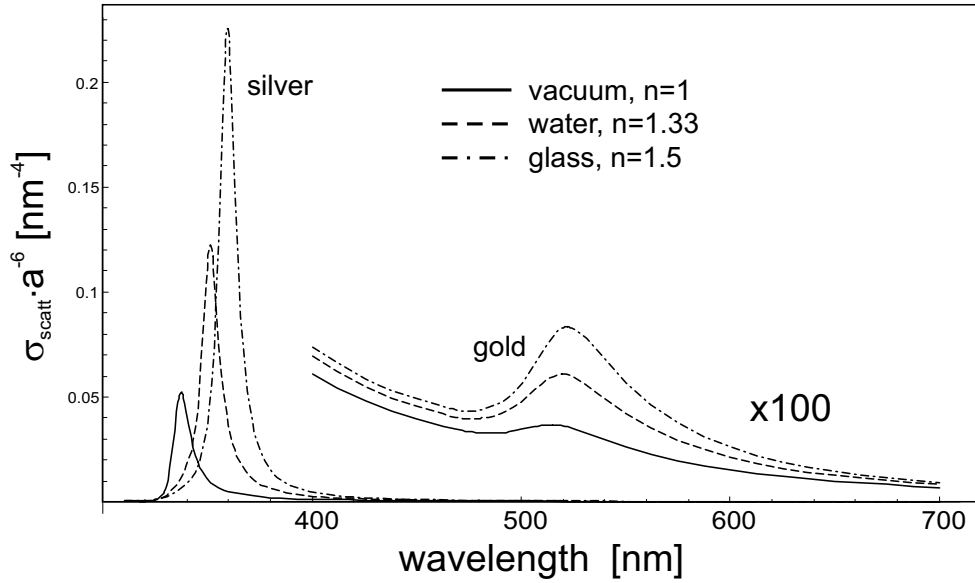


Figure 12.19: Plots of the scattering cross-section of spherical gold and silver particles in different environments normalized by a^6 , with a denoting the particle radius. In the current example, $a=20$ nm. Solid line: vacuum ($n=1$). Dashed line: water ($n=1.33$). Dash-dotted line: glass ($n=1.5$).

greenish color. A very nice illustration of these findings are colored glasses. The famous Lycurgus cup shown in Fig. 12.20 was made by ancient roman artists and is today exhibited at the British Museum, London. When illuminated by a white source from behind, the cup shows an amazingly rich shading of colors ranging from deep green to bright red. For a long time it was not clear what causes these colors. Today it is known that they are due to nanometer-sized gold particles embedded in the glass. The colors are determined by an interplay of absorption and scattering.

Local interactions with particle plasmons

The resonance condition of a particle plasmon depends sensitively on the dielectric constant of the environment. Thus, similar to the case of a plane interface, a gold or silver particle can be used as a sensing element since its resonance will shift upon local dielectric changes, e.g. due to the specific binding of certain ligands after chemical functionalization of the particle's surface. The advantage of using particle resonances as opposed to resonances of plane interfaces is associated with the much smaller dimensions of the particle and hence the larger surface to volume ratio. One can envision to anchor differently functionalized particles onto substrates at extremely high densities and use such arrangements as sensor chips for multiparameter sensing of various chemical compounds, as demonstrated by the detection of single base pair mismatches in DNA (see e.g. [34]). Resonance shifts of small noble metal particles

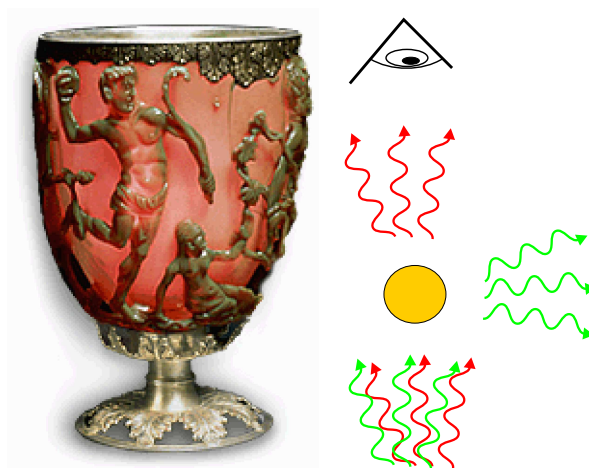


Figure 12.20: Ancient roman Lycurgus cup illuminated by a light source from behind. Light absorption by the embedded gold particles leads to a red color of the transmitted light whereas scattering at the particles yields a greenish color. From <http://www.thebritishmuseum.ac.uk/science/lycurguscup/sr-lycugus-p1.html>.

were also applied in the context of near-field optical microscopy. The observation of the resonance shift of a metal particle as a function of a changing environment was already demonstrated by Fischer and Pohl in 1989 [35]. Similar experiments were performed later using gold particles attached to a tip [36]. The type of setup and the particular probe used is discussed in more detail in chapter 6.

12.4.2 Plasmon resonances of more complex structures

Because of their high symmetry, simple structures such as isolated small spheres exhibit a single plasmon resonance. However, more complex structures often yield multi-featured resonance spectra and strongly enhanced local fields in gaps between or at intersection points of different particles [41]. Simple arguments can be applied to provide a qualitative understanding of more complex plasmon resonances and their geometrical dependence. In fact, plasmon resonances of complex structures can be viewed as the result of a "hybridization" of elementary plasmons of simpler substructures [37]. To give an example, consider the resonances of a hollow metallic shell as shown in Fig. 12.21 (a). The elementary resonances of this particle are found by decomposition into a solid metal sphere and a spherical cavity in bulk metal. Fig. 12.21 (b) shows how the elementary modes can be combined to form hybrids. A low energy (red-shifted) hybrid mode is obtained for an in-phase oscillation of the elementary plasmons whereas the anti-phase combination represents a higher-energy mode that is blue-shifted. The degree of interaction between the elementary modes is determined by the spatial separation of the modes (shell thickness) [42].

Similar considerations can be adopted to understand the multiple plasmon resonances that occur for asymmetric particles such as e.g. pairs of metal particles. Here, besides the hybridization effect, different resonances can occur for different directions of polarization of the excitation light. For example, consider a pair of spherical particles as sketched in Fig. 12.22 (a)-(c). The elementary plasmon resonance (a) is

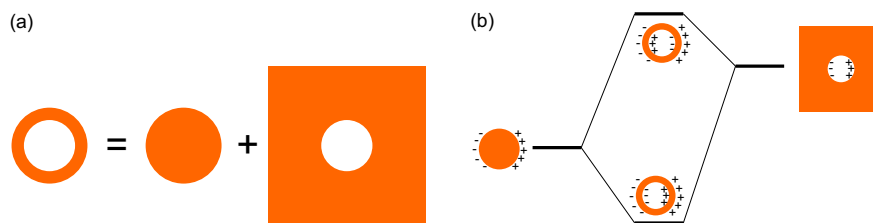


Figure 12.21: Generation of multi-featured surface plasmon resonances by hybridization of elementary modes for the example of a gold nanoshell [37]. (a) Elementary structures, (b) Energies of elementary and hybridized modes.

hybridized when two particles are sufficiently close such that the dipole of one particle induces a dipole in the other particle. Possible hybrid modes of the combined structure are sketched in Fig. 12.22 (b) and (c). For different polarizations, different modes of the system are excited which may shift to lower or higher energies for increased coupling. For example, the low energy modes of Fig. 12.22 (b) and (c) shift to the red, respectively to the blue, for decreasing inter particle distances. This is because for decreasing distance in the first case the opposite charges close to the gap reduce the energy of the configuration whereas in the second case the overall energy (Coulomb repulsion) is increased [43, 44].

In a similar manner the multi-featured resonances of single asymmetric and complex-shaped particles can be understood. Fig. 12.22 (d) shows simulated field distributions at the resonance frequency near a metallic nanowire with triangular cross-section

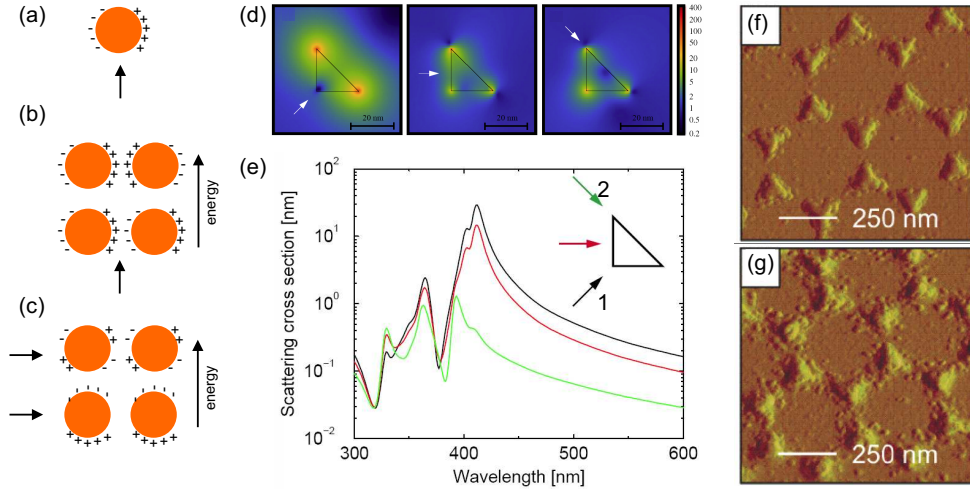


Figure 12.22: Shape effects in particle plasmon resonances. (a) Elementary mode of a spherical particle. The arrow indicates the polarization direction of the exciting field. (b),(c) Surface charge distributions of hybrid plasmon modes associated with particle pairs. The polarization direction is perpendicular (b) and parallel (c) to the long axis of the particle axis. (d) Near-field distribution of resonant silver nanowires with triangular cross-sections. The polarization direction is indicated by white arrows. (e) Scattering spectra corresponding to the distributions shown in (d). From [38] without permission. (f) and (g) show AFM images of triangular resonant silver particles created by nanosphere lithography used for the detection of Alzheimer's disease. (g) is without attached antibodies and (f) is with attached antibodies. From [39] without permission.

when illuminated from different directions indicated by the white arrows [38]. The resulting scattering spectra are displayed in Fig. 12.22 (e). As expected from the two-particle model discussed before, the resonance region for excitation in direction 1 (black spectrum) is red-shifted with respect to the resonance region obtained for excitation along direction 2 (green spectrum). Triangular-shaped silver particles show very high sensitivity of their spectral properties to changes of the dielectric constant of their environment. Fig. 12.22 (f) and (g) show AFM images of triangular silver patches created by nanosphere lithography [45, 46]. Upon attachment of specific antibodies (g) the resonance of the particle shifts notably [39] which can be exploited for sensitive detection of minute amounts of analyte. An important problem in 'plasmonics' is the question of how metal particles should be designed and arranged with respect to each other to produce the strongest possible field enhancement.

One possible solution to this problem is the configuration of a self-similar chain of particles with decreasing diameters [40] as depicted in Fig. 12.23. Self similarity requires that radii R_i and the distances $d_{i,i+1}$ of the spheres i and $i+1$ are connected by the simple relations $R_{i+1} = \kappa R_i$ and $d_{i+1,i+2} = \kappa d_{i,i+1}$ where $\kappa \ll 1$. The last condition ensures that the field of a given nanoparticle is only a weak perturbation of the previous, bigger particle. The self-similarity is not a necessary condition but it allows for an elegant notation. All particles are considered in the electrostatic limit. Now, if

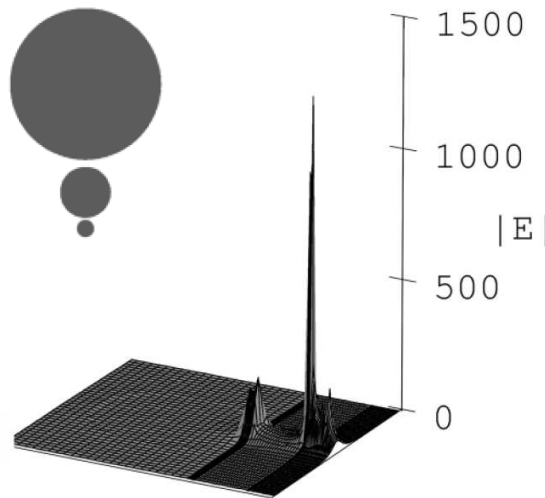


Figure 12.23: Self-similar chain of metallic nanoparticles. A very strong resonance is observed for an excitation wavelength of $\lambda = 381.5$ nm. The associated field enhancement in the gap between the two smallest spheres is larger than 1000. From [40] without permission.

each of the particles enhances its driving field by a certain factor α , then the cumulative effect of the chain of particles is a field enhancement on the order of α^n where n is the number of particles. In other words, the enhanced field of the largest particle acts as an excitation field for the next smaller particle. The resulting enhanced field of this second particle then acts as the excitation field for the next smaller particle, and so on. For the system depicted in Fig. 12.23, assuming a moderate $\alpha \sim 10$, leads to a total field enhancement of ~ 1000 [40]. As we will see in the following section, field enhancements of at least 1000 are necessary to observe the Raman scattering of single molecules adsorbed onto rough metal structures.

12.4.3 Surface-enhanced Raman scattering

The energy spectrum of molecular vibrations can serve as an unambiguous characteristic fingerprint for the chemical composition of a sample. Due to its sensitivity to molecular vibrations, Raman scattering spectroscopy is a very important tool for the analysis of nanomaterials. Raman scattering is named after Sir Chandrasekhara V. Raman who first observed the effect in 1928 [47]. Raman scattering can be viewed as a mixing process similar to amplitude modulation used in radio signal transmission: the time-harmonic optical field (the carrier) is mixed with the molecular vibrations (the signal). This mixing process gives rise to scattered radiation that is frequency-shifted from the incident radiation by an amount that corresponds to the vibrational frequencies of the molecules (ω_{vib}). The vibrational frequencies originate from oscillations between the constituent atoms of the molecules and, according to quantum mechanics, these oscillations persist even at ultralow temperatures. Because the vibrations depend on the particular molecular structure the vibrational spectrum constitutes a characteristic fingerprint of a molecule. A formal description based on quantum electrodynamics can be found in Ref. [48]. Fig. 12.24 shows the energy level diagrams for Stokes and anti-Stokes Raman scattering together with an experimentally measured spectrum for Rhodamine 6G.

It is not the purpose of this section to go into the details of Raman scattering but it is important to emphasize that Raman scattering is an extremely weak effect. The Raman scattering cross-section is typically 14 – 15 orders of magnitude smaller than the fluorescence cross-section of efficient dye molecules. The field enhancement associated with surface plasmons, as described above, has hence been extensively explored for increasing the interaction-strength between a molecule and optical radiation. The most prominent example is surface enhanced Raman scattering (SERS).

In 1974 it was reported that the Raman scattering cross-section can be considerably increased if the molecules are adsorbed on roughened metal surfaces [49]. In the following decades SERS became an active research field [50]. Typical enhancement factors for the Raman signal observed from rough metal substrates as compared to

bare glass substrates are on the order of $10^6 - 10^7$, and using resonance enhancement (excitation frequency near an electronic transition frequency) enhancement factors as high as 10^{12} have been reported. The determination of these enhancement factors was based on ensemble measurements. However, later two independent *single molecule* studies reported giant enhancement factors of 10^{14} [51, 52]. These studies not only shed new light on the nature of SERS but made Raman scattering as efficient as fluorescence measurements (cross-sections of $\approx 10^{-16} \text{ cm}^2$). The interesting outcome of these single molecule studies is that the average enhancement factor coincides with previous ensemble measurements, but while most of the molecules remain unaffected by the metal surface only a few make up for the detected signal. These are the molecules with the giant enhancement factors of 10^{14} . These molecules are assumed to be located in a favorable local environment (hot spots) characterized by strongly enhanced electric fields.

Despite all the activity in elucidating the physical principles underlying SERS, a satisfactory theory explaining the fundamental origin of the effect is still missing. It is accepted that the largest contribution to the giant signal enhancement stems from the enhanced electric fields at rough metal surfaces. Highest field enhancements are found in junctions between metal particles or in cracks on surfaces (see e.g. [51, 41]). It is commonly assumed that the Raman scattering enhancement scales with the

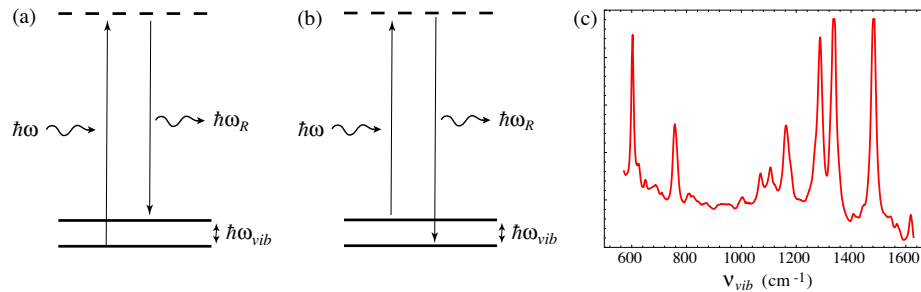


Figure 12.24: Raman scattering refers to the spectroscopic process in which a molecule absorbs a photon with frequency ω and subsequently emits a photon at a different frequency ω_R which is offset with respect to ω by a vibrational frequency ω_{vib} of the molecule, i.e. $\omega_R = \omega \pm \omega_{vib}$. Absorption and emission are mediated by a virtual state, i.e. a vacuum state that does not match any molecular energy level. (a) If $\omega > \omega_R$ one speaks of Stokes Raman scattering, and (b) if $\omega < \omega_R$ the process is designated as anti-Stokes Raman scattering. (c) Raman scattering spectrum representing the vibrational frequencies of Rhodamine 6G. The spectrum is expressed in wavenumbers $\nu_{vib}(\text{cm}^{-1}) = [1/\lambda(\text{cm})] - [1/\lambda_R(\text{cm})]$, with λ and λ_R being the wavelengths of incident and scattered light, respectively.

fourth power of the electric field enhancement factor. At first glance this seems odd as one would expect that this implies that Raman scattering is a nonlinear effect scaling with the square of the excitation intensity. However, this is not so. In the following we will provide a qualitative explanation based on a scalar phenomenological theory. It is straightforward to rigorously expand this theory but the mathematical details would obscure the physical picture. Notice, that the theory outlined in the following is not specific to Raman scattering but applies also to any other linear interaction such as Rayleigh scattering and fluorescence.[§]

Let us consider the situation depicted in Fig. 12.25. A molecule located at \mathbf{r}_o is placed in the vicinity of metal nanostructures (particles, tips, ..) that act as a local field enhancing device. The interaction of the incident field E_o with the molecule gives rise to a dipole moment associated with Raman scattering according to

$$\mu(\omega_R) = \alpha(\omega_R, \omega) [E_o(\mathbf{r}_o, \omega) + E_s(\mathbf{r}_o, \omega)] , \quad (12.51)$$

where ω is the frequency of the exciting radiation and ω_R is a particular vibrationally shifted frequency ($\omega_R = \omega \pm \omega_{vib}$). The polarizability α is modulated at the vibrational frequency ω_{vib} of the molecule and gives rise to the frequency mixing process. The molecule is interacting with the local field $E_o + E_s$, where E_o is the local field in absence of the metal nanostructures and E_s is the enhanced field originating from the interaction with the nanostructures (scattered field). E_s depends linearly on the excitation field E_o and hence it can be qualitatively represented as $f_1(\omega)E_o$, with f_1 designating the field enhancement factor.

The electric field radiated by the induced dipole μ can be represented by the system's Green's function G , which accounts for the presence of the metal nanostructures,

[§]In case of fluorescence, one needs to take into account that the excited-state lifetimes can be drastically reduced near metal surfaces.

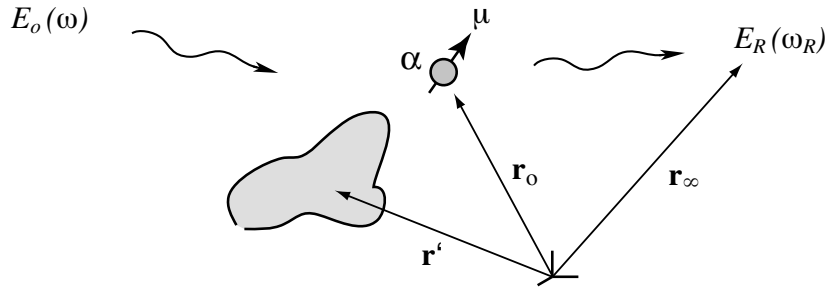


Figure 12.25: General configuration encountered in surface enhanced spectroscopy. The interaction between a molecule with polarizability α and the exciting field E_o gives rise to a scattered field E_R . Placing metal nanostructures (coordinate \mathbf{r}') near the molecule enhances both the exciting field and the radiated field.

as

$$E(\mathbf{r}_\infty, \omega_R) = \frac{\omega_R^2}{\varepsilon_o c^2} G(\mathbf{r}_\infty, \mathbf{r}_o) \mu(\omega_R) = \frac{\omega_R^2}{\varepsilon_o c^2} [G_o(\mathbf{r}_\infty, \mathbf{r}_o) + G_s(\mathbf{r}_\infty, \mathbf{r}_o)] \mu(\omega_R). \quad (12.52)$$

Similar to the case of the exciting local field, we split the Green's function into a free-space part G_o (absence of metal nanostructures) and a scattered part G_s originating from the interaction with the metal nanostructures. We represent G_s qualitatively as $f_2(\omega_R)G_o$, with f_2 being a second field enhancement factor.

Finally, combining Eqs. (12.51) and (12.52), using the relations $E_s = f_1(\omega)E_o$, and $G_s = f_2(\omega_R)G_o$, and calculating the intensity $I \propto |E|^2$ yields

$$I(\mathbf{r}_\infty, \omega_R) = \frac{\omega_R^4}{\varepsilon_o^2 c^4} \left| [1 + f_2(\omega_R)] G_o(\mathbf{r}_\infty, \mathbf{r}_o) \alpha(\omega_R, \omega) [1 + f_1(\omega)] \right|^2 I_o(\mathbf{r}_o, \omega). \quad (12.53)$$

Thus, we find that the Raman scattered intensity scales linearly with the excitation intensity I_o and that it depends on the factor

$$\left| [1 + f_2(\omega_R)][1 + f_1(\omega)] \right|^2. \quad (12.54)$$

In absence of any metal nanostructures, we obtain the scattered intensity by setting $f_1 = f_2 = 0$. On the other hand, in presence of the nanostructures we assume that $f_1, f_2 \gg 1$ and hence the overall Raman scattering enhancement becomes

$$f_{Raman} = \left| f_2(\omega_R) \right|^2 \left| f_1(\omega) \right|^2, \quad (12.55)$$

Provided that $|\omega_R \pm \omega|$ is smaller than the spectral response of the metal nanostructure the Raman scattering enhancement scales roughly with the fourth power of the electric field enhancement. It should be kept in mind that our analysis is qualitative and it ignores the vectorial nature of the fields and the tensorial properties of the polarizability. Nevertheless, a rigorous self-consistent formulation along the here outlined steps is possible. Besides the described field enhancement mechanism, additional enhancements associated with SERS are a short-range 'chemical' enhancement which results from the direct contact of the molecule with the metal surface. This direct contact results in a modified ground-state electronic charge distribution which gives rise to a modified polarizability α . Further enhancement can be accomplished through resonant Raman scattering for which the excitation frequency is near an electronic transition frequency of the molecule, i.e. the virtual levels shown in Fig. 12.24 come close to an electronic state of the molecule.

Over the past decades, a lot of effort has been dedicated to SERS but the progress has been challenged by the experimental difficulties associated with the fabrication of well-defined and reproducible metal nanostructures. New developments in nanofabrication and characterization and the availability of sensitive instrumentation that

allow us to study a single molecule at a time promise that the SERS puzzle be resolved in the near future.

12.5 Conclusion

In this chapter we have discussed the basic properties of surface plasmons. We have pointed out the nature of these modes as being a hybrid between local optical fields and associated electron density waves in a metal. As nano-optics in general deals with optical fields in the close vicinity of (metallic) nanostructures it is obvious that such collective excitations play a major role in the field. There exist many applications and prospects of surface plasmons that we could not mention here. The study of plasmons on metal nanostructures has developed into a research field of its own called "plasmonics". For more information, the interested reader is referred to e.g. [53-55] and references therein.

Problems

Problem 12.1 Study the effect of a complex dielectric function on the propagation of a plane wave. What happens if a plane wave is normally incident on a metal interface?

Problem 12.2 Show that for an Ansatz similar to Eq. (12.11), however, with s-polarized waves, a reflected wave has to be added to fulfill the boundary conditions and Maxwell's equations simultaneously.

Problem 12.3 Show that if we do not demand the solution to be a surface wave, i.e. if the perpendicular wave vector, Eq. (12.18), may be real, then we arrive at the well known condition for the Brewster effect.

Problem 12.4 Write a small program that plots the reflectivity of a system of (at least up to 4) stratified layers as a function of the angle of incidence using the notation of (12.14). Study a system consisting of glass, gold, and air with a thickness of the gold layer of about 50 nm between an glass and a gold half space. Plot the reflectivity for light incident from the glass side and from the air side. What do you observe? Study the influence of thin layers of additional materials on top or below the gold. A few nanometers of Titanium or Chromium are often used to enhance the adhesion of gold to glass. What happens if a monolayer of proteins (~ 5 nm in diam., refractive index ~ 1.33) is adsorbed on top of the gold layer?

Hint

Consider a stratified layer of thickness d (medium 1) between 2 homogeneous half spaces (medium 0 and 2). According to (12.14) the fields in each medium for p-polarization read as

$$\mathbf{E}_0 = E_0^+ \begin{pmatrix} 1 \\ 0 \\ -\frac{k_x}{k_{0,z}} \end{pmatrix} e^{ik_{0,z}z} + E_0^- \begin{pmatrix} 1 \\ 0 \\ \frac{k_x}{k_{0,z}} \end{pmatrix} e^{-ik_{0,z}z} \quad (12.56)$$

$$\mathbf{E}_1 = E_1^+ \begin{pmatrix} 1 \\ 0 \\ -\frac{k_x}{k_{1,z}} \end{pmatrix} e^{ik_{1,z}z} + E_1^- \begin{pmatrix} 1 \\ 0 \\ \frac{k_x}{k_{1,z}} \end{pmatrix} e^{-ik_{1,z}(z-d)} \quad (12.57)$$

$$\mathbf{E}_2 = E_2^+ \begin{pmatrix} 1 \\ 0 \\ -\frac{k_x}{k_{2,z}} \end{pmatrix} e^{ik_{2,z}(z-d)} \quad (12.58)$$

Exploiting the continuity of \mathbf{E}_{\parallel} and \mathbf{D}_{\perp} yield after some manipulation

$$\begin{pmatrix} E_0^+ \\ E_0^- \end{pmatrix} = \frac{1}{2} \begin{pmatrix} 1 + \kappa_1 \eta_1 & 1 - \kappa_1 \eta_1 \\ 1 - \kappa_1 \eta_1 & 1 + \kappa_1 \eta_1 \end{pmatrix} \begin{pmatrix} 1 & 0 \\ 0 & e^{ik_{1,z}d} \end{pmatrix} \begin{pmatrix} E_1^+ \\ E_1^- \end{pmatrix} \quad (12.59)$$

as well as

$$\begin{pmatrix} E_1^+ \\ E_1^- \end{pmatrix} = \begin{pmatrix} e^{-ik_{1,z}d} & 0 \\ 0 & 1 \end{pmatrix} \frac{1}{2} \begin{pmatrix} 1 + \kappa_2\eta_2 & 1 - \kappa_2\eta_2 \\ 1 - \kappa_2\eta_2 & 1 + \kappa_2\eta_2 \end{pmatrix} \begin{pmatrix} E_2^+ \\ 0 \end{pmatrix} \quad (12.60)$$

where $\kappa_i = k_{i,z}/k_{i+1,z}$ and $\eta_i = \varepsilon_{i+1}/\varepsilon_i$. Eqns. (12.59) and (12.60) can be combined to give

$$\begin{pmatrix} E_0^+ \\ E_0^- \end{pmatrix} = \mathbf{T}_{0,1} \cdot \Phi_1 \cdot \mathbf{T}_{1,2} \begin{pmatrix} E_2^+ \\ 0 \end{pmatrix}. \quad (12.61)$$

Here

$$\mathbf{T}_{0,1} = \frac{1}{2} \begin{pmatrix} 1 + \kappa_1\eta_1 & 1 - \kappa_1\eta_1 \\ 1 - \kappa_1\eta_1 & 1 + \kappa_1\eta_1 \end{pmatrix} \quad (12.62)$$

and

$$\mathbf{T}_{1,2} = \frac{1}{2} \begin{pmatrix} 1 + \kappa_2\eta_2 & 1 - \kappa_2\eta_2 \\ 1 - \kappa_2\eta_2 & 1 + \kappa_2\eta_2 \end{pmatrix} \quad (12.63)$$

and

$$\Phi_1 = \begin{pmatrix} e^{-ik_{1,z}d} & 0 \\ 0 & e^{ik_{1,z}d} \end{pmatrix}. \quad (12.64)$$

From this we can infer a general relation connecting the fields outside an arbitrary system of stratified layers which reads as

$$\begin{pmatrix} E_0^+ \\ E_0^- \end{pmatrix} = \mathbf{T}_{0,1} \cdot \Phi_1 \cdot \mathbf{T}_{1,2} \cdot \Phi_2 \cdot \dots \cdot \mathbf{T}_{n,n+1} \begin{pmatrix} E_{n+1}^+ \\ 0 \end{pmatrix}. \quad (12.65)$$

The reflectivity $R(\omega, k_x)$ can be calculated from (12.65) as

$$R(\omega, k_x) = \frac{|E_0^-|^2}{|E_0^+|^2} \quad (12.66)$$

from which E_{n+1}^+ cancels out.

Problem 12.5 Extend the program you have just written to determine the amount of intensity enhancement obtained right above the metal layer by determining the ratio between the incoming intensity and the intensity right above the metal layer.

Problem 12.6 Prove that Eq. (12.28) actually is exactly the electrostatic field of a point dipole, only that it oscillates in time with $e^{i\omega t}$.

Problem 12.7 Solve the Laplace equation (12.41) for a spherical particle and verify the results (12.45) and (12.46).

References

- [1] M. Born and E. Wolf. *Principles of Optics*. Cambridge University Press, Cambridge, sixth edition, 1980.
- [2] C.F. Bohren and D.R. Huffman. *Absorption and scattering of light by small particles*. Wiley science paperback series. John Wiley & Sons, Inc., New York, 1983.
- [3] R.E. Hummel. *Optische Eigenschaften von Metallen und Legierungen*. Number 22 in Reine und angewandte Metallkunde in Einzeldarstellungen. Springer Verlag, Berlin, Heidelberg, New York, 1971.
- [4] T. Okamoto. *Near-field optics and surface plasmon polaritons*, volume 81 of *Topics in Applied Physics*, pages 97–122. Springer, 2001.
- [5] N.W. Ashcroft and N.D. Mermin. *Solid state Physics*. Saunders College, Philadelphia, PA 19105, hwr international edition edition, 1976.
- [6] P. B. Johnson and R. W. Christy. Optical constants of the noble metals. *Phys. Rev. B* **6**, 4370–4379 (1972).
- [7] C. Sönnichsen. *Plasmons in metal nanostructures*. Cuvillier Verlag, Göttingen, 2001.
- [8] K. Welford. The method of attenuated total reflection. In *Surface Plasmon Polaritons*, volume 9 of *IOP Short Meetings Series*, pages 25–78. IOP Publishing Ltd, 1987.
- [9] H. Raether. *Surface Plasmons on Smooth and Rough Surfaces and on Gratings*, volume 111 of *Springer Tracts in Modern Physics*. Springer Verlag, Berlin Heidelberg, 1988.
- [10] O. Marti, H. Bielefeldt, B. Hecht, S. Herminghaus, P. Leiderer, and J. Mlynek. Near-field optical measurement of the surface plasmon field. *Optics Commun.* **96**, 225–228 (1993).
- [11] E. T. Arakawa, M. W. Williams, R. N. Hamm, and R. H. Ritchie. *Phys. Rev. Lett.* **31**, 1127–1130 (1973).
- [12] A. Otto. Excitation of nonradiative surface plasma waves in silver by the method of frustrated total reflection. *Z. Phys.* **216**, 398–410 (1968).
- [13] E. Kretschmann. *Z. Phys.* **241**, 313 (1971).
- [14] H.J. Lezec, A. Degiron, E. Devaux, R.A. Linke, L. Martin-Moreno, F.J. Garcia-Vidal, and T.W. Ebbesen. Beaming light from a subwavelength aperture. *Science* **297**, 820–822 (2002).

-
- [15] B. Liedberg, C. Nylander, and I. Lundstrom. Surface-plasmon resonance for gas-detection and biosensing. *Sensors and actuators* **4**, 299–304 (1983).
- [16] J. Homola, S.S. Yee, and G. Gauglitz. Surface plasmon resonance sensors: review. *Sensors and Actuators B* **54**, 3–15 (1999).
- [17] B. Hecht, H. Bielefeldt, L. Novotny, Y. Inouye, and D.W. Pohl. Local excitation, scattering, and interference of surface plasmons. *Phys. Rev. Lett.* **77**, 1889–1893 (1996).
- [18] L. Novotny, B. Hecht, and D.W. Pohl. Interference of locally excited surface plasmons. *J. Appl. Phys.* **81**, 1798–1806 (1997).
- [19] J. R. Lakowicz. Radiative decay engineering 3. surface plasmon-coupled directional emission. *Anal. Biochem.* **324**, 153–169 (2004).
- [20] H. Ditlbacher, J.R.Krenn, N. Felidj, B. Lamprecht, G. Schider, M. Salerno, A. Leitner, and F.R. Aussenegg. Fluorescence imaging of surface plasmon fields. *Appl. Phys. Lett.* **80**, 404–406 (2002).
- [21] B. Hecht, D. W. Pohl, and L. Novotny. Local excitation of surface plasmons by "TNOM". *NATO Series E: 'Optics at the Nanometer Scale: Imaging and Storing with Photonic Near Fields'*, eds. M. Nieto-Vesperinas and N. Garcia, Kluwer Academic Publishers, Dordrecht, 319:151–161, 1996.
- [22] E. Matveeva, Z. Gryczynski, I. Gryczynski, and J. Malicka and J. R. Lakowicz. Myoglobin immunoassay utilizing directional surface plasmon-coupled emission. *Angew. Chem.* **76**, 6287–6292 (2004).
- [23] S.I. Bozhevolnyi and V. Coello. Elastic scattering of surface plasmon polaritons: Modelling and experiment. *Phys. Rev. B* **58**, 10899–10910 (1998).
- [24] A. Bouhelier, Th. Huser, H. Tamaru, H.-J. Gntherodt, D.W. Pohl, F.I. Baida, and D. Van Labeke. Plasmon optics of structured silver films. *Phys. Rev. B* **63**, 155404 (2001).
- [25] H. Ditlbacher, J.R. Krenn, G. Schider, A. Leitner, and F.R. Aussenegg. Two-dimensional optics with surface plasmon polaritons. *Appl. Phys. Lett.* **81**, 1762–1764 (2002).
- [26] J. R. Krenn, B. Lamprecht, H. Ditlbacher, G. Schider, M. Salerno, A. Leitner, and F. R. Aussenegg. Nondiffraction-limited light transport by gold nanowires. *Europhys. Lett.* **60**, 663–669 (2002).
- [27] J.-C. Weeber, A. Dereux, C. Girard, J. R. Krenn, and J.-P. Goudonnet. Plasmon polaritons of metallic nanowires for controlling submicron propagation of light. *Phys. Rev. B* **60**, 9061–9068 (1999).

-
- [28] M. Kerker. *The scattering of light and other electromagnetic radiation*. Academic Press, New York, p. 84 1969.
- [29] G.B. Arfken and H.J. Weber. *Mathematical methods for Physicists*. Academic Press, San Diego, London, 1995.
- [30] L. Novotny and C. Hafner. Light propagation in a cylindrical waveguide with a complex, metallic, dielectric function. *Phys. Rev. E* **50**, 4094–4106 (1994).
- [31] M. I. Stockman. Nanofocusing of optical energy in tapered plasmonic waveguides. *Phys. Rev. Lett.* **93**, 137404 (2004).
- [32] D. Hondros. Über elektromagnetische Drahtwellen. *Ann. d. Physik* **30**, 905–950 (1909).
- [33] D. Boyer, Ph. Tamarat, A. Maali, B. Lounis, and M. Orrit. Photothermal Imaging of Nanometer-Sized Metal Particles Among Scatterers. *Science* **297**, 1160–1163 (2002).
- [34] S. J. Oldenburg, C. C. Genicka, K. A. Clarka, and D. A. Schultz. Base pair mismatch recognition using plasmon resonant particle labels. *Anal. Biochem.* **309**, 109–116 (2003).
- [35] U.Ch. Fischer and D.W. Pohl. Observation on single-particle plasmons by near-field optical microscopy. *Phys. Rev. Lett.* **62**, 458 (1989).
- [36] T. Kalkbrenner, M. Ramstein, J. Mlynek, and V. Sandoghdar. A single gold particle as a probe for apertureless scanning near-field optical microscopy. *Journal of Microscopy* **202**, 72–76 (2001).
- [37] E. Prodan, C. Radloff, and N. J. Halas nad P. Nordlander. A hybridization model for the plasmon response of complex nanostructures. *Science* **302**, 419–422 (2003).
- [38] J. Kottmann, O.J.F. Martin, D. Smith, and S. Schultz. Spectral response of plasmon resonant nanoparticles with a non-regular shape. *Opt. Express* **6**, 213–219 (2000).
- [39] A. J. Haes, W. P. Hall, L. Chang, W. L. Klein, and R. P. Van Duyne. A localized surface plasmon resonance biosensor: First steps toward an assay for alzheimers disease. *Nano Letters* **4**, 1029–1034 (2004).
- [40] K. Li, M. I. Stockman, and D. J. Bergman. Self-similar chain of metal nanospheres as an efficient nanolens. *Phys. Rev. Lett.* **91**, 227402 (2003).
- [41] A. M. Michaels, J. Jiang, and L. Brus. Ag nanocrystal junctions as the site for surface-enhanced raman scattering of single rhodamine 6g molecules. *J. Phys. C.* **104**, 11965–11971 (2000).

-
- [42] J.B. Jackson, S.L. Westcott, L.R. Hirsch, J.L. West, and N.J. Halas. Controlling the surface enhanced raman effect via the nanoshell geometry. *Appl. Phys. Lett.* **82**, 257–259 (2003).
- [43] J. P. Kottmann and O. J. F. Martin. Plasmon resonant coupling in metallic nanowires. *Opt. Express* **8**, 655–663 (2001).
- [44] W. Rechberger, A. Hohenau, A. Leitner, J.R. Krenn, B. Lamprecht, and F. R. Aussenegg. Optical properties of two interacting gold nanoparticles. *Optics Commun.* **220**, 137–141 (2003).
- [45] H. W. Deckman and J. H. Dunsmuir. Natural lithography. *Appl. Phys. Lett.* **41**, 377–379 (1982)
- [46] J. C. Hulthen and R. P. Van Duyne. Nanosphere lithography: A materials general fabrication process for periodic particle array surfaces. *J. Vac. Sci. Technol. A* **13**, 1553–1558 (1994).
- [47] C. V. Raman and K. S. Krishnan, “A new type of secondary radiation,” *Nature* **121**, 501 (1928).
- [48] M. Diem, *Introduction to Modern Vibrational Spectroscopy*, Wiley-Interscience (1993).
- [49] M. Fleischmann, P. J. Hendra, and A. J. McQuillan, “Raman spectra of pyridine adsorbed at a silver electrode,” *Chem. Phys. Lett.* **26**, 163 (1974).
- [50] A. Otto, I. Mrozek, H. Grabhorn, and W. Akemann, “Surface enhanced Raman scattering,” *J. Phys.: Condens. Matter* **4**, 1143 (1992).
- [51] S. Nie and S. R. Emory, “Probing single molecules and single nanoparticles by surface enhanced Raman scattering,” *Science* **275**, 1102 (1997).
- [52] K. Kneipp, Y. Wang, H. Kneipp, I. Itzkan, R. R. Dasary, and M. S. Feld, “Single molecule detection using surface enhanced Raman scattering (SERS),” *Phys. Rev. Lett.* **78**, 1667 (1997).
- [53] S. Kawata, editor. *Near-field optics and surface plasmon polaritons*, volume 81 of *Topics in Applied Physics*. Springer, Berlin, 2001.
- [54] W.L. Barnes, A. Dereux, and T.W. Ebbesen. Surface plasmon subwavelength optics. *Nature* **424**, 824–830 (2003).
- [55] J.B. Pendry, L. Martin-Moreno, and F.J. Garcia-Vidal. Mimicking surface plasmons with structured surfaces. *Science* **305**, 847–848 (2004).